The Wind-Blown Sand Experiment in the Empty Quarter Desert: Roughness Length and Saltation Characteristics

Narendra Nelli, Diana Francis, Mamadou Sow, Ricardo Fonseca, Abdulrahman Alkatheeri, Emmanuel Bosc, Gilles Bergametti

Earth and Space Science

RESEARCH ARTICLE
10.1029/2024EA003512

The Wind-Blown Sand Experiment in the Empty Quarter Desert: Roughness Length and Saltation Characteristics

Narendra Nelli[1], Diana Francis[1], Mamadou Sow[2], Ricardo Fonseca[1], Abdulrahman Alkatheeri[1], Emmanuel Bosc[3], and Gilles Bergametti[4]

[1]Environmental and Geophysical Sciences (ENGEOS) Lab, Earth Science Department, Khalifa University, Abu Dhabi, United Arab Emirates, [2]Institut de Radioprotection et de Sûreté Nucléaire (IRSN), PSN-RES, SCA, LPMA, Gif-sur-Yvette Cedex, France, [3]Federal Authority for Nuclear Regulation (FANR), Abu Dhabi, United Arab Emirates, [4]CNRS, LISA, Université Paris Est Créteil and Université Paris Cité, Créteil, France

Abstract The Empty Quarter Desert, one of Earth's major dust sources, frequently experiences dust storms due to wind erosion. Despite its significance as a primary dust source on a global scale, in-situ observations from this region had not been reported until very recently. In summer 2022, the WInd-blown Sand Experiment (WISE) Phase-1 was initiated in the Empty Quarter Desert of the United Arab Emirates, and continued until 7 February 2023. Utilizing a diverse array of instruments, we measured winds, temperature, humidity, radiation fluxes, saltation, and the physical and optical properties of dust aerosols, atmospheric electric fields, and soil characteristics. A total of 38 distinct sand-saltation events were recorded from September 2022 to February 2023, with activity peaking between 13:00 and 14:00 local time. Key findings include the identification of dominant wind patterns, and the measurement of the average aerodynamic roughness length (z_0) at 0.8 ± 0.6 mm, and the thermal roughness length (z_h) at 0.3 ± 0.5 mm—the first estimation of z_h for this area. In-situ observations revealed that dust particle concentrations near the surface increased 1.7-fold on days with saltation compared to days without it. Moreover, we determined a wind-speed threshold for initiating saltation at 7.70 m s^{-1}. This comprehensive data set significantly advances our understanding of atmospheric-soil interactions and sand movement dynamics, providing invaluable insights for ongoing research into desert environments and the global dust cycle.

Plain Language Summary The Empty Quarter Desert, one of the Earth's major dust sources, frequently experiences dust storms due to wind erosion. Despite its importance as a main dust source on a global scale, no in-situ observations from this region have been reported until very recently. In the summer of 2022, the WInd-blown Sand Experiment (WISE) Phase-1 provided crucial data on the arid environment of the Empty Quarter Desert in the United Arab Emirates. Lasting until February 2023, this experiment focused on quantifying environmental and soil characteristics through an array of measurements, including wind direction and speed, temperature, humidity, radiation fluxes, and dust particle concentrations. The study revealed dominant wind patterns, quantified the aerodynamic and thermal roughness of the desert soil, and recorded 38 distinct sand movement events, noting a peak in activity during early afternoon hours. This research is significant for its detailed analysis of particle concentration changes during these events and its establishment of a specific wind speed threshold for sand movement in this region. These findings are invaluable for researchers studying desert environments, particularly in terms of understanding atmospheric-soil interactions and the dynamics of sand movement.

Key Points:

- First-of-its kind experiment in the Empty Quarter Desert to characterize environmental dynamics
- The first estimation of the thermal roughness length (z_h) for this desert and is found to be 0.3 mm
- The derived wind-speed threshold for saltation at the Empty Quarter Desert is 7.70 m s^{-1}

Supporting Information:

Supporting Information may be found in the online version of this article.

Correspondence to:

D. Francis,
diana.francis@ku.ac.ae

Citation:

Nelli, N., Francis, D., Sow, M., Fonseca, R., Alkatheeri, A., Bosc, E., & Bergametti, G. (2024). The wind-blown sand experiment in the Empty Quarter Desert: Roughness length and saltation characteristics. *Earth and Space Science*, *11*, e2024EA003512. https://doi.org/10.1029/2024EA003512

Received 4 JAN 2024
Accepted 17 MAY 2024

Author Contributions:

Conceptualization: Narendra Nelli, Diana Francis
Data curation: Narendra Nelli, Abdulrahman Alkatheeri
Formal analysis: Narendra Nelli, Diana Francis, Mamadou Sow, Ricardo Fonseca
Funding acquisition: Diana Francis
Methodology: Mamadou Sow
Project administration: Diana Francis, Emmanuel Bosc
Resources: Emmanuel Bosc
Supervision: Diana Francis
Validation: Diana Francis, Ricardo Fonseca, Gilles Bergametti
Visualization: Narendra Nelli, Abdulrahman Alkatheeri

1. Introduction

The Empty Quarter Desert, also known as the Rub' al Khali, is the largest contiguous sand desert in the world, covering approximately 650,000 km^2 in the Arabian Peninsula, including parts of Saudi Arabia, Oman, the United Arab Emirates (UAE) and Yemen. It is characterized by extremely low and erratic precipitation, high temperature variations and variable winds, making it a harsh and challenging environment for life and human activity (Nelli et al., 2022). Despite its inhospitable conditions, the Empty Quarter serves as a natural laboratory for studying aeolian processes such as sand transport, dune formation, and dust emission that have significant impacts on the local and global environments. One of the most remarkable aeolian phenomena in the Empty Quarter is the frequent occurrence of dust storms. Dust storms originating from the Rub Al Khali desert have the highest aerosol

Writing – original draft: Narendra Nelli
Writing – review & editing: Narendra Nelli, Diana Francis, Ricardo Fonseca

optical depth and contribute the most to the local dust emissions in the Arabian Peninsula region (Al-Hemoud et al., 2022; Notaro et al., 2013).

Saltation is a key process in aeolian research, where sand particles move through leaps and bounds. This movement plays a significant role in shaping dunes, wearing down bedrock, and causing soil erosion in arid and semiarid areas (Tan et al., 2020). This process is driven by gusty winds, leading to variable patterns in both time and space, making it nonuniform and unpredictable. A foundational aspect of understanding aeolian transport is identifying the onset of saltation, defined by the threshold wind speed required for particles to become airborne. This threshold is essential not only for understanding sand movement but also for identifying the initiation of airborne dust, which has considerable environmental implications.

The implications of these emissions are manifold. They are capable of modifying regional weather and associated mesoscale processes, such as the Arabian Heat Low (AHL; Fonseca et al., 2022), Mesoscale Convective Systems (MCSs; Nelli, Francis, et al., 2021), temperature inversions, and land-sea breeze circulations (e.g., Francis, Nelli, et al., 2022, 2023; Weston et al., 2021). Francis et al. (2021) reported on a large dust storm over the Empty Quarter Desert in July 2018 associated with the development of a dry cyclone, which lifted dust to more than 5 km above the surface and was associated with AODs in excess of 3, with model-predicted dust loads of 20 Tg. As dust is known to block the incoming shortwave (SW) radiation from the Sun and enhance the downward longwave (LW) radiation flux, and when compared to non-dusty days, the air temperature is generally cooler during the day and warmer at night. In this particular event a nighttime warming of up to $+10°C$ and a daytime cooling of up to $-3°C$ was observed at two stations in the UAE. In addition to its impact on mesoscale circulations, the dry cyclone promoted the development of convection over the Al Hajar mountains of the UAE and Oman. Using the Weather Research and Forecasting (WRF) model (Skamarock et al., 2019), Fonseca et al. (2021) analyzed a summertime convective event in the UAE and determined that variations in dust loading played a role in the behavior of the AHL, its interplay with sea-breeze circulations, and the resulting locations of convection development. The Empty Quarter Desert is known to contribute significantly to the global dust budget, with dust plumes from the region frequently crossing international borders and affecting air quality and climate in neighboring countries and beyond (e.g., Al-Hemoud et al., 2022; Francis, Fonseca, & Nelli, 2022).

Existing regional models have demonstrated limitations in accurately capturing these complex dynamics. They exhibit biases in predicting radiative fluxes, air temperature, and wind speeds, largely due to inaccuracies in representing dust loading. For example, and for the July 2018 dust storm over the Empty Quarter Desert, Francis et al. (2021) noted that their model overestimated the reduction in the surface SW radiation flux by 300 W m^{-2} or roughly a third of its value, and overestimated the downward and upward LW radiation fluxes by up to 100 and 50 W m^{-2}, respectively. Such discrepancies underscore the critical need for long-term, in-situ measurements for enhancing numerical model accuracy and for the evaluation of satellite data products, particularly in the presence of surface-level or elevated dust layers. The presence of dust also has implications in the satellite detection of surface and near-surface features, as highlighted by Weston et al. (2021).

Dust emission in arid and semi-arid regions is mainly driven by wind and its interactions with soil surface. Thus, surface characteristics such as roughness, soil particles size distribution, moisture, crust, etc.; play an important role (Bagnold, 1941; Chepil, 1951; Fécan et al., 1999; Gillette et al., 2001; Iversen & White, 1982). In fact, in commonly used dust parameterization schemes, a threshold value of roughness length is used above which no emission occurs so as to prevent dust emission in urban and vegetated regions (LeGrand et al., 2023). What is more, the soil water content and clay mass fraction, the terrain elevation and the surface albedo also typically modulate the threshold speed for dust emission in numerical models (LeGrand et al., 2023). Field measurements show that saltation (the horizontal sand motion) is a prerequisite for significant dust emissions (Gunn et al., 2021; Shao et al., 2011; Sow et al., 2009). In addition, studies including those by Kok and Renno (2006) and Esposito et al. (2016) have shown that the sand grains movement threshold is affected by the electric field generated by the tribocharging of the grains due to their collision on each other during erosive events.

In-situ measurements of dust emission flux during aeolian erosion events remain rare, despite their importance in evaluating and improving dust emission schemes in dust models (e.g., Dupont et al., 2021; Marticorena & Bergametti, 1995; Shao et al., 2011; Sow et al., 2009). Given the wide size distribution of dust particles and their diverse responses to flow eddies, measuring dust emission flux poses considerable challenges. However, a comprehensive understanding of emitted dust size distribution is paramount for estimating dust impacts on atmospheric components and processes (e.g., Alfaro et al., 1998; Mahowald et al., 2014). In order to gain more

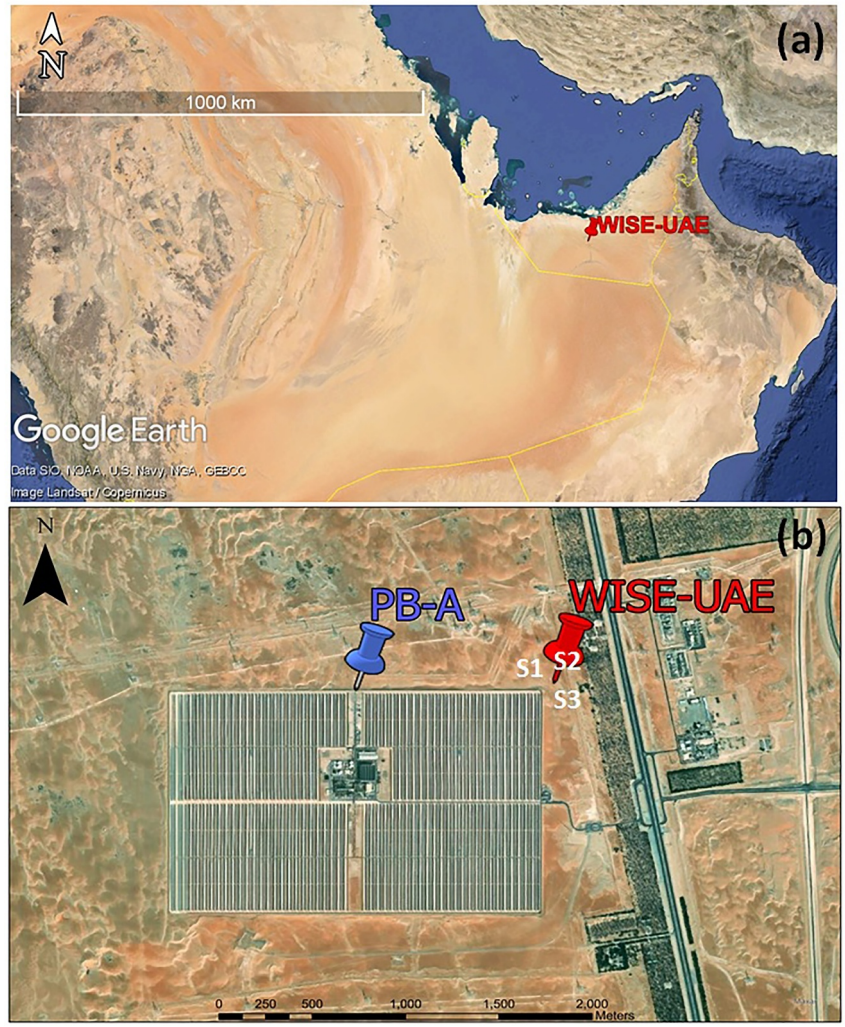

Figure 1. WInd-blown Sand Experiment (WISE)-United Arab Emirates (UAE) Site. (a) The WISE-UAE location in the United Arab Emirates (Google Earth). (b) Close-up view of the study area. The red pin gives the location of the 10-m micrometeorological tower (23.5761°N, 53.7242°E) and the blue pin indicates the northern end of the SHAMS solar power plant. The prevailing wind directions at the site are marked in (b) as follows: Sector-1 (280°-320°) labeled as S1, Sector-2 (20°-50°) labeled as S2, and Sector-3 (210°-100°) labeled as S3.

knowledge about the Empty Quarter Desert environment, we have conceived and conducted comprehensive measurements during the *WInd-blown Sand Experiment (WISE)* in the Empty Quarter Desert in the UAE. Here, we discuss the first results of this experiment and we derive from in-situ measurements the atmospheric characteristics of this environment such as the aerodynamic roughness length (z_0) and thermal roughness length (z_h), saltation diurnal cycle and wind-speed threshold for saltation.

In this paper, we first introduce the *WISE-UAE* experiment site and instrumentation in Section 2, prevailing weather conditions during the *WISE-UAE*, diurnal variability in meteorological parameters, estimations of aerodynamic and thermal roughness lengths, and wind speed threshold for saltation are discussed in Section 3. A summary of the main findings is given in Section 4.

2. Implementation of WISE-UAE

2.1. Experiment Site Description

The WISE experiment was conducted at Madinat Zayed (23.5761°N, 53.7242°E; elevation: 119 m) located 120 km south-west of Abu Dhabi, UAE (Figure 1a). The ground surface is flat with a fetch of more than 300-m in

the maximum prevailing wind direction (Figure 1b). The soil type, loamy sand, is very prone to wind erosion. Before the start of the experiment, the site was leveled with a shovel truck over an area of approximately 2,300 m^2 to ensure an ideal, flat surface of bare soil without soil crust or ridges. X-ray diffraction analysis was utilized to determine the mineralogical composition of sand samples from the site. The results highlight a dominant presence of quartz, making up 55% of the sample. Calcite is the next major component, comprising 18%, followed by the Plagioclase or Albite fraction, which amounts to 13%. The three constituents present in smaller amounts are K-Feldspar or Microcline and Dolmite, which account for 11% and 3% of the sample, respectively. This mineral composition is similar to that of other deserts such as the Taklimakan Desert in Asia (Honda & Shimizu, 2002) and the Sahara Desert in North Africa (Pastore et al., 2021).

To characterize the prevailing wind direction at the site, the wind speed and wind direction measurements at the northern end of the solar power plant, blue pin in Figure 1b, for the period 2014–2020 are summarized in Figure 2. It is noted that there are three prevailing wind directions sectors for all months: sector-1, northwesterly winds, 280°–320°; sector-2, northeasterly, 20°–50°; sector-3, south-southwest to easterly, 210°–100°. The strongest speeds occur for sector-1 winds and can exceed 9 m s^{-1}, they are associated with the large-scale flow in the region (Nelli et al., 2020b). The north-westerly winds, often referred to as "Shamal," form due to the movement of baroclinic extra-tropical weather systems during colder months. In warmer periods, they emerge due to the sharp pressure difference between the thermal low spreading west from India and Pakistan and the subtropical high pressure spanning from the eastern Mediterranean to northern Saudi Arabia (Kumar et al., 2015; Yu et al., 2016). The peak speeds occur in June, when the aforementioned pressure gradient is the steepest, before the breakdown of the monsoon low in July (Al Senafi & Anis, 2015). Furthermore, the sea-breeze circulation contributes to the emergence of northwesterly winds, complementing the prevailing background currents (Eager et al., 2008). Winds from Sector-2 and Sector-3 are associated with land-breeze circulation, usually showcasing speeds less than 3 m s^{-1}. It should be noted that the solar plant is situated approximately 110 m southwest of our measurement site, which ensures that the predominant wind directions do not intersect with the location of the solar plant. Additionally, our wind speed measurements taken at 10 m yield a fetch-to-height ratio of over 11:1, which exceeds the typically recommended 10:1 ratio for accurate wind speed measurements over a homogeneous, flat surface (Panofsky & Townsend, 1964).

2.2. Instrumentation

An overview of the WISE-UAE experimental setup and the comprehensive instrumentation used during the experiment are provided in Figure 3 and Table 1, respectively. The 10-m high micrometeorological tower has the shape of a triangle with horizontal booms fitted at seven heights (0.4, 0.7, 1.25, 2.25, 3, 4, 10 m above the ground) for mounting the 2-D sonic anemometer sensors, all in one weather sensor, and radar precipitation sensor. One horizontal boom with supporting boom is fitted at 3 m height for mounting the 3-D sonic anemometer (Figure 3a). The tower is anchored with the three Guy Wires and can withstand wind speeds up to 60 m s^{-1}. In order to measure the four components of the radiation fluxes (namely downward and upward shortwave and longwave), a Net Radiometer is installed on a separate 2-m high tripod, at a distance of 4-m to the south of the tower (Figure 3b). The electric field is measured with a Campbell CS110 electric field mill facing down and installed at 2-m high in the southwest direction of the tower (Figure 3b). The electrical connection of the reciprocating shutter to the ground potential is ensured by a flexible stainless-steel strap. This connection is further strengthened by attaching the metallic support mast to a 1.5 m copper bar, which is deeply embedded in the ground. The CS110 measures the vertical component of the electric field, E_z, within a range of −25 to 25 kV m^{-1}, recording data every second (Nelli et al., 2024). It's capable of detecting both cloud-to-ground and cloud-to-cloud lightning events up to a distance of approximately 40 km (25 miles). Instead of using the rotating-vane mechanism found in traditional field mills, the CS110 employs a reciprocating shutter that alternates its position by 45° during the reading process. This design not only ensures accurate electric field recordings but also reduces the need for frequent maintenance. Additionally, the CS110 has built-in self-diagnostic features, offering status flags for every measurement it takes.

In order to investigate the dust emissions during wind erosion, two optical particle counters (OPCs, GRIMM 1.108) and two nephelometers (DataRAM 4 Data-logging Real-time Aerosol Monitor 4, Model DR-4000) were deployed (Figure 3c). The OPCs measures the dust particles in 15 size-classes ranging from 0.3 to 20 μm (namely 0.3–0.4, 0.4–0.5, 0.5–0.65, 0.65–0.80, 0.8–1.0, 1.0–1.6, 1.6–2.0, 2.0–3.0, 3.0–4.0, 4.0–5.0, 5.0–7.5, 7.5–10, 10–15, 15–20, >20 μm). The nephelometer measures the dust mass concentration up to 400 mg m^{-3}.

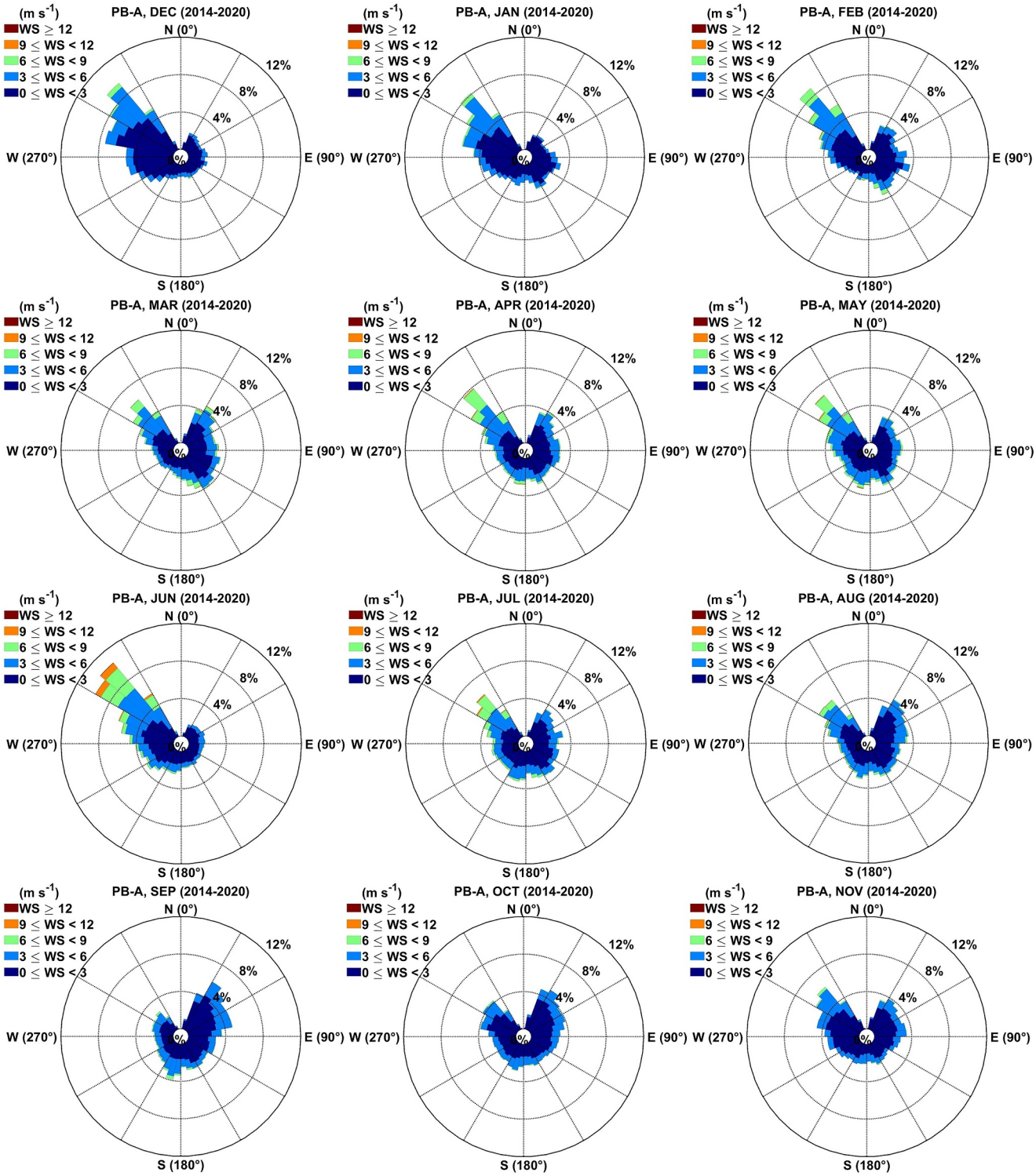

Figure 2. Wind direction and wind speed at WInd-blown Sand Experiment-United Arab Emirates site. Prevailing monthly wind direction and respective speed (m s^{-1}) at the northern end of the solar power plant (blue pin in Figure 1a) for 2014–2020.

The two sets of instruments are first calibrated in the lab, before being operated at the same height for nearly 12 hr to intercompare the measurements. To calculate the dust emission fluxes utilizing the gradient approach (Sow et al., 2009), the sampling heads of OPC and nephelometer are placed at 2- and 4-m heights (Figure 3c).

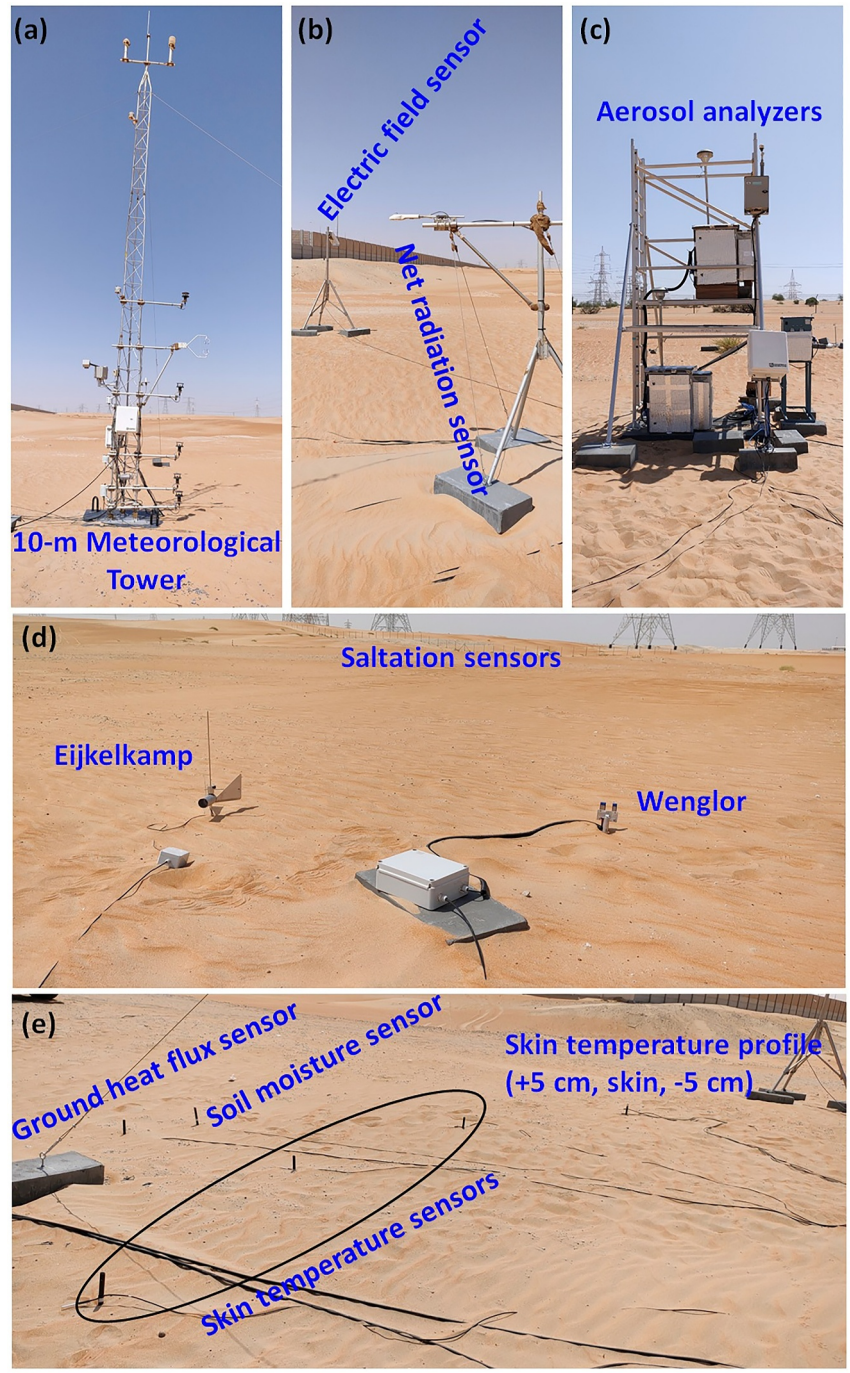

Figure 3. WInd-blown Sand Experiment-United Arab Emirates experiment setup. (a) 10 m meteorological tower showing all the instruments deployed on it. (b) Net radiation (foreground) and electric field (background) sensors. (c) Outdoor enclosures, with aerosol analyzers installed inside, and dust profiler. Ground sensors (d) saltation sensors and (e) soil temperature, soil moisture and ground heat flux.

In addition to these one dust profiler (Aeroqual) is installed on a scaffold at 4-m height (Figure 3c). Aeroqual's dust analyzer continuously measures particulates, including PM10, PM2.5, PM1, and Total Suspended Particulate. The device employs an OPC to categorize and tally particulate matter based on size, then translates this size distribution into a mass reading. Due to the failure of the motor pump, the dust profiler functioned only until November 2022.

Table 1
Instruments Deployed During the WInd-Blown Sand Experiment-United Arab Emirates Field Campaign

S. no.	Instrument (make and model)	Measured parameters	Measurement height and sampling interval
1	2-D sonic anemometer (Gill,60)	Wind speed and Wind direction	Five levels (0.4, 0.7, 1.25, 2.25, 4 m from the surface) 1 min
2	Temperature and RH sensor (Campbell Scientific, HygroVUE10)	Temperature and Relative humidity	Five levels (0.4, 1, 2, 4, 8 m) 1 min
3	All in one weather sensor (Lufft, WS501)	Temperature and RH, Wind speed and wind direction, Global Solar radiation, air pressure	10 m 1 min
4	Radar Precipitation Sensor/Smart Disdrometer (Lufft, WS100)	Precipitation and precipitation type	10 m 1 min
5	3-D sonic anemometer (Campbell Scientific, CSAT3B-SS2-SC)	Three components of wind speed (u,v,w) and Sonic temperature	3 m 5 and 20 Hz
6	Pressure sensor (Vaisala, CS106)	Atmospheric pressure	1 m 1 min
7	Net Radiometer (Kipp and Zonen, CNR4)	Four components of radiation fluxes (upward and downward SW and LW radiation fluxes)	2 m 1 min
8	Soil heat flux sensor (Hukseflux, HFP01)	Ground heat flux	−15 cm below the surface 5 Hz
9	Soil temperature sensor (Campbell Scientific, 107-33-PT)	Soil temperature	Six sensors were installed at four locations separated by 2 m distance Location-1: +5 cm, skin, −5 cm Location-2: skin Location-3: skin Location-4: skin 1 min
10	Soil moisture sensor (Campbell Scientific, CS655)	Soil moisture	Installed at −5 cm below the surface with a separation distance of 1 m from heat flux sensor 1 min
11	Saltiphone (Wenglor Fork sensor; Model: YH03PCT8)	Saltation count	+9 cm from the surface 1 s
12	Saltiphone (Eijkelkamp)	Saltation count	+9 cm from the surface 1 s
13	Electric Field sensor (Campbell Scientific, CS110)	Atmospheric electric field	2 m height 1 s
14	Visibility sensor (Sentry™, Model 73000S)	Horizontal visibility	2.5 m height 1 min
15	Optical Particle Counter (OPC, GRIMM 1.108)	Particle number concentration for 15 channels in the range 0.3–20 μm	2 and 4 m 1 min
16	Nephelometer (DataRAM4 (Data-logging Real-time Aerosol Monitor 4), Model: DR-4000)	Mass concentration	2 and 4 m 1-min
17	Dust profiler (Aeroqual)	PM1, PM2.5, PM10, TSP	4 m height 1 min
18	MWAC Sand trap	Sand sample	Two masts separated by 3 m distance Five levels (5, 10, 20, 40, 80 cm)

Table 1
Continued

S. no.	Instrument (make and model)	Measured parameters	Measurement height and sampling interval
19	Data loggers (Campbell Scientific, CR1000X)	The data for all instruments except DATARAM4 is logged in CR1000X and transmitted via cellular modem to the Khalifa University data server	Two

Note. For each instrument, the measured parameters, and specifications are given.

In order to characterize saltation of sand (beginning, end, and intensity) at the site, Saltiphone (Eijkelkamp®, Giesbeek, the Netherlands) and Wenglor optical gate sensor (Wenglor, Sensoric GmbH, Germany, Model: YH03PCT8, 655 nm laser and photosensor 30 m apart), is placed at distance of 10-m from the tower, approximately 9-cm above the surface to prevent the overloading of the sensor (Figure 3d). Eijkelkamp's Saltiphone operates by counting the collisions of saltating particles on a microphone surface, as described by Spaan and Van den Abeele (1991). Conversely, the Wenglor fork sensor features a U-shaped design housing both a transmitter (laser) and a receiver (photo sensor). The sensor registers a decrease in signal voltage when moving grains disrupt the laser beam, which has a 30 mm length and 1 mm diameter. Davidson-Arnott et al. (2009) initially applied the Wenglor for aeolian research. Its effectiveness in quantifying sand particle saltation has been thoroughly assessed in various studies, including those by Barchyn and Hugenholtz (2010), Hugenholtz and Barchyn (2011), Sherman et al. (2011), Barchyn et al. (2014), and Bauer et al. (2018). The saltation hits (counts/second) from both the saltation sensors for every 1 s are logged in a CR1000X data-logger-2. A Wenglor fork sensor is fixed to sample the air in a specific direction, in our case from the northwest to the southeast, which aligns with the predominant wind direction. In contrast, the Saltiphone is capable of sampling air from any direction as it can rotate in response to changes in wind direction. To maintain consistency in our saltation measurements, we meticulously manage the height of the soil surface around the saltation sensors. After each significant saltation event, and routinely every 2 weeks, we conducted site visits to ensure that the soil surface was leveled around the saltation sensors. This procedure was critical in preserving the constant sensing height required for accurate data collection from our saltation sensors throughout Phase-1 of the WISE-UAE campaign.

To quantify horizontal erosion fluxes, Modified Wilson and Coke (MWAC) sand traps consisting of bottles mounted on a pole, at five levels (5, 10, 20, 40, 80 cm), outfitted with a sail to guarantee the inlet always faced the wind direction, were set up. Two sand traps are located in the northeast direction, 20-m from the tower, and placed 3-m from each other. The sand captured in the bottles is collected once every fortnight and weighed. The collected sand samples undergo additional analysis to determine the mineral composition. The SEN-TRY™ Visibility Sensors 1 (SVS1) instrument is employed for visibility measurements. Mounted at 2.5 m on the 10-m tower, the sensor operates by determining the scatter of visible light by the atmosphere. This allows for the calculation of the extinction coefficient, μ, which represents the attenuation of a beam from aerosol scattering and absorption. Detailed information about this tool can be found in SENTRYTM (2019) and Temimi, Fonseca, Nelli, Valappil, et al. (2020).

Several ground sensors, namely ground heat flux plate, soil temperature (location 1: soil temperature profile at a height of +5 cm which gives air temperature, skin just above the surface, and −5 cm below the ground; locations 2–4: skin temperature measurements with horizontal separation of 2 m) and soil moisture sensor are installed at a distance of roughly 10-m from the tower, between its south and south-southwest quadrants (Figure 3d).

Two Campbell Scientific, CR1000X, data loggers are used to log the measurements. The instruments listed from S. no. 1 to 10 in Table 1 are connected to logger-1, which is attached to the 10-m mast. For those listed as S.No 11 to 15, the data is logged in logger-2, which is installed on the scaffold. Data logged in both the data loggers is transmitted to the Khalifa University's data server using two cellular modems. At Khalifa University, the logger net software is used to receive the transmitted data. The DataRAM4 and Dust profiler data is logged in locally on datatap and SD cards, respectively. Once every fortnight, we visit the site and manually download the data from the nephelometers and dust profilers. To power the WISE-UAE instrumentation, a 3-phase electric cable of length 800 m is laid from the SHAMS convectional center to the field site.

In addition to the in-situ observations, two satellite-derived products were utilized for this study: (1) Merged Infrared Brightness Temperatures (IRBT) from the National Center for Environmental Prediction (NCEP)/

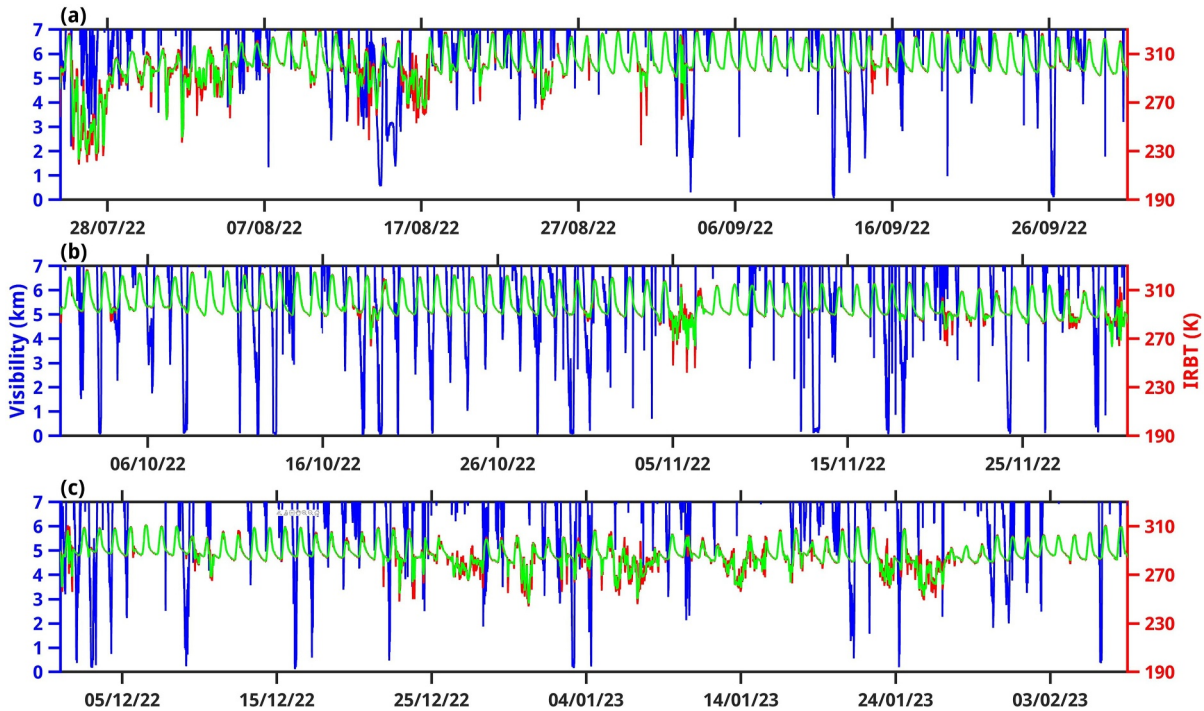

Figure 4. Day-to-day visibility and Infrared Brightness Temperatures (IRBT) during WInd-blown Sand Experiment-United Arab Emirates (UAE) field campaign. The blue line gives the horizontal visibility (km), the green line the averaged IRBT within a 25 km radius of the WISE-UAE location (K) and the red line the IRBT at the closest grid-point to the field site from 25 July 2022 to 7 February 2023.

Climate Prediction Center (CPC) obtained from a combination of geostationary satellite products provided by European, Japanese, and United States agencies. The IRBT data is accessible every 30 min on a 4 km grid that spans from 60°S to 60°N (https://disc.gsfc.nasa.gov/datasets/GPM_MERGIR_1/summary). Additionally, the Spinning Enhanced Visible and Infrared Imager (the Spinning Enhanced Visible and Infrared Imager (SEVIRI) tool) tool on the Meteosat Second Generation spacecraft provides Dust and Fog Red-Green-Blue (RGB) imagery (https://navigator.eumetsat.int/product/EO:EUM:DAT:MSG:HRSEVIRI-IODC/print) every 15 min, boasting a spatial precision of roughly 3 km at the sub-satellite location. The reanalysis data sets employed are the European Center for Medium Range Weather Forecasting's (ECMWF) ERA-5 (Hersbach et al., 2018a, 2018b, 2019a, 2019b) for the atmospheric fields. ERA-5 data, available on an hourly basis and at a spatial resolution of 0.25° × 0.25° (~27 km) from 1950 to present, is selected as it is one of the best performing reanalysis in the Middle East and South Asia (Fonseca et al., 2022; Mahto & Mishra, 2019).

3. Results

In this section, we provide a description of the prevailing weather conditions during the experimental period, which spanned from 25 July 2022 to 7February 2023. Following that, we estimate the aerodynamic and thermal roughness lengths at the WISE-UAE location. All times are Local Time (LT) (UTC + 4) unless otherwise stated.

3.1. Background Weather Conditions During WISE-UAE Phase-1

We examined the background weather conditions during the WISE-UAE campaign by combining the 10-m tower data with satellite-derived products. Figure 4 illustrates the variability in horizontal visibility and the averaged IRBT for an area encompassing a 25 km radius around the WISE-UAE location.

IRBT is a widely recognized metric utilized to infer convection on regional and global scales (e.g., Machado et al., 1998; Nelli, Francis, et al., 2021; Nelli et al., 2022; Rao et al., 2013; Reddy & Rao, 2018). In order to discern cloud types at the WISE-UAE site, we adopted the IRBT thresholds specified by Rao et al. (2013) and Reddy and Rao (2018). According to these, highly convective clouds correspond to IRBT values below 210 K, while very deep convective clouds are identified by values ranging from 210 to 235 K. An IRBT range of 235–260 K

Table 2
List of Convective Occurrences and Dust Episodes, and Windy Days Throughout the WInd-Blown Sand Experiment-United Arab Emirates Field Campaign

S. no.	Weather condition	Date
1	Deep and very deep convection	25–27 July 2022
		1 August 2022
		31 December 2022
		7 January 2022
		25 January 2022
2	Dust storm	14 August 2022
3	Strong northwesterly windy days	16 September 2022
		20 November 2022
		10, 28–29 December 2022
		3, 28 January 2023

suggests the presence of deep convective clouds, while mid-level clouds are associated with a range of 260–270 K. IRBT values between 270 and 280 K imply the presence of cirrus or low-level clouds, whereas values exceeding 280 K point to clear skies. Convective events with duration 2 hr or more are listed in Table 2.

Dust storms and fog are detected using horizontal visibility measurements taken at the site, along with dust and fog RGB satellite images. Dust incidents are categorized as follows: Severe Dust Storm (with a horizontal visibility ranging from 0 to 200 m), Dust Storm (horizontal visibility between 200 m and 1 km), and Dust Event (horizontal visibility between 1 and 5 km). In addition to horizontal visibility and dust RGB imagery, we take into account the prevailing weather conditions, denoting the atmospheric events observed at a specific station during that time (Basha et al., 2019). During the first phase of WISE-UAE, a single dust storm was observed, which took place on 14 August 2022, and lasted approximately 3.5 hr (Table 2).

During the first phase of WISE-UAE, the experimental site underwent 7 days of intense northwesterly winds, which are associated with Shamal events (Table 2 and Figure 5). According to Yu et al. (2016) and Li and Sadr (2023), a Shamal day at a specific location is characterized by vigorous north-northwesterly winds, with meteorological wind directions ranging between 270° and 30°, and a wind speed exceeding 7.1 m s^{-1}. This wind speed threshold corresponds to the 97th percentile of all recorded observations. These conditions need to prevail for a minimum of 25% of all daytime observations (6–18 LT) to qualify the day as a Shamal day (Li & Sadr, 2023; Yu et al., 2016). The day-to-day variability of the hourly-averaged 10-m wind speed and wind direction is summarized in Figure 5.

The experiment site predominantly experiences wind directions from the northwest to northeast (sea-breeze) and southeast (land-breeze), with the former associated with stronger wind speeds. During Phase-1 of the WISE-UAE campaign, the mean wind speeds in these dominant sectors (280°–50°, 100°–210°) were 3.3 ± 2.0 and 2.5 ± 1.9 ms^{-1}, respectively. Low wind speeds (<4 m s^{-1}) prevailed during the majority of the time

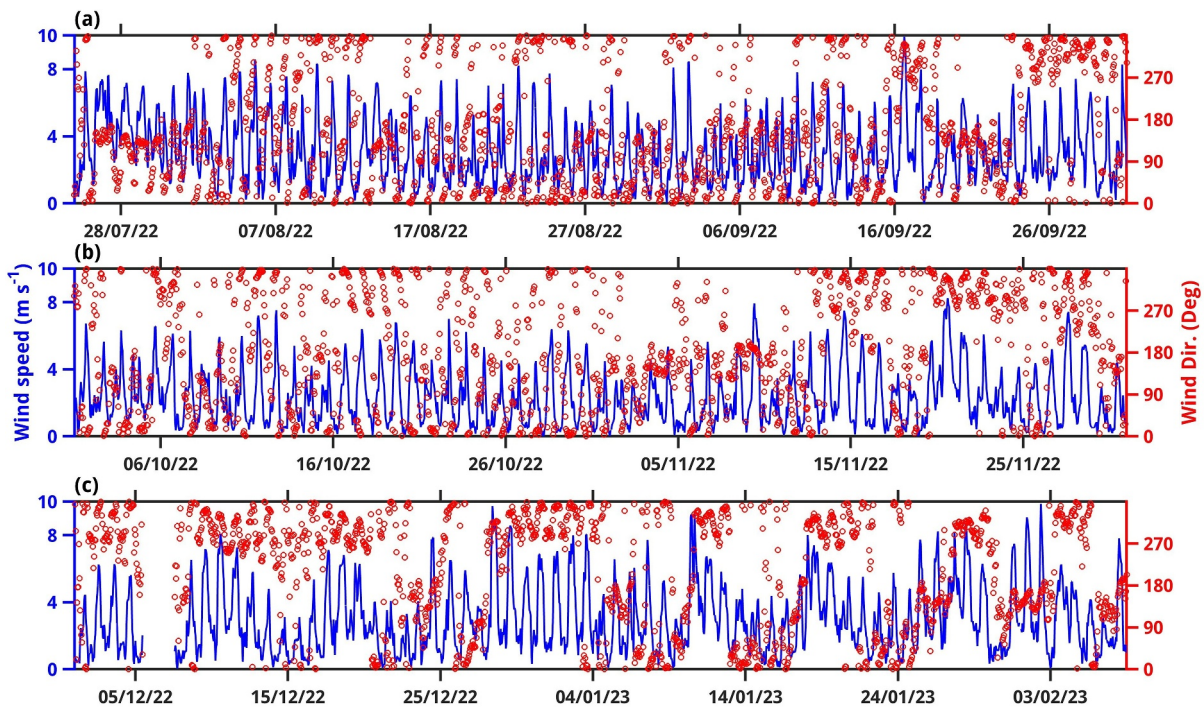

Figure 5. Observed 10-m wind during WInd-blown Sand Experiment (WISE)-United Arab Emirates field campaign. Hourly-averaged wind speed (m s^{-1}) and direction (°) at a 10-m height at the WISE location during (a) 25 July–30 September 2022, (b) 1 October–30 November 2022 and (c) 1 December 2022–7 February 2023.

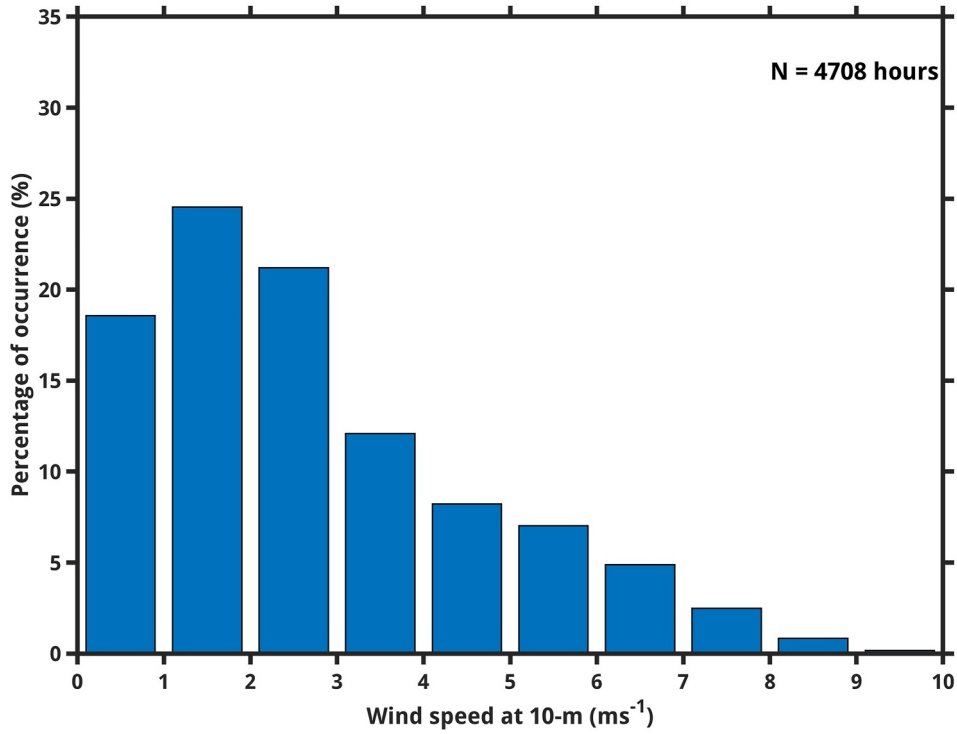

Figure 6. Wind speed distribution at WInd-blown Sand Experiment-United Arab Emirates site. Frequency of occurrence of wind speeds (m s^{-1}) at a 10-m height in different wind speed range bins.

(Figure 6). The frequency of wind speeds ≥4 m s^{-1} (<4 m s^{-1}) is 23.6% (76.4%), which is lower than at the Barakah coastal location (Nelli et al., 2022). The maximum (mean) hourly averaged wind speed recorded during the campaign was 9.9 ms^{-1} (2.8 ± 1.9 ms^{-1}). Interestingly, diurnal variations in wind speed were observed at the SHAMS site on all days, regardless of the background synoptic conditions. This observation is expected, as the SHAMS location is further inland compared to other coastal locations, such as Barakah and Abu Dhabi. Previous studies conducted at Barakah reported the persistent occurrence of strong northwesterly winds for several days when the location is under the influence of favorable synoptic conditions (Abida et al., 2022; Nelli et al., 2022; Weston et al., 2022).

Fog is a weather phenomenon that occurs when horizontal visibility falls below a typical benchmark of 1,000 m due to the suspension of water droplets in the air. This study determines fog events using metrics such as horizontal visibility and relative humidity (RH). Initially, fog occurrence times are detected during periods when the horizontal visibility is less than or equal to 1 km and RH is greater than 93% (e.g., Fonseca et al., 2023; Nelli et al., 2022; Temimi, Fonseca, Nelli, Valappil, et al., 2020; Thota et al., 2020; Weston et al., 2022). Subsequently, a visual inspection of 15-min SEVIRI Fog RGB images is conducted to confirm the presence of fog at the detected times. Furthermore, cloudy or rainy conditions are filtered out using the 30-min merged IRBT data from geostationary satellites averaged around the WISE-UAE location (Nelli, Francis, et al., 2021; Reddy & Rao, 2018), Figure 4, and the radar precipitation sensor installed at 10-m height. Table 3 provides a detailed list of each fog occurrence, including the date, onset time, duration, minimum horizontal visibility, and average horizontal wind speed at 10-m height for each fog event. Note that very short-lived fog occurrences, with durations less than 15 min, are excluded from the analysis. Throughout the observed period, a total of 27 fog events were recorded, each varying in duration from 28 min to approximately 8 hr and 41 min. Visibility during these events ranged from 41.8 to 470 m. The average wind speed during the fog events was 0.9 ± 0.4 m s^{-1}, consistent with the speeds given in Figure 5. The longest-lasting fog event occurred on 13 November 2022. The changes in the atmospheric electric field during these foggy events are studied by Nelli et al. (2024). According to the study of Weston and Temimi (2020), the area around SHAMS is one of the most fog-prone regions in the UAE, with an average of 60–70 fog days in the 10-month period December 2016–March 2017 and October 2017–March 2018 as inferred from satellite data.

Table 3
Fog Occurrence at WInd-Blown Sand Experiment (WISE)-United Arab Emirates (UAE) Site

	Fog occurrence timings				
S. no.	Start date	Onset (local time)	Duration (hh:mm)	Minimum horizontal visibility (m)	Average horizontal wind speed (m s^{-1})
1	3-September-2022	03:44	00:28	305.4	0.9
2	12-September-2022	04:29	02:45	68.5	1.0
3	26-September-2022	03:26	04:26	99.0	1.9
4	3-October-2022	04:54	03:01	64.8	1.9
5	8-October-2022	00:51	04:39	92.5	0.7
6	11-October-2022	05:59	00:28	108.3	1.2
7	12-October-2022	06:10	02:16	36.3	0.7
8	13-October-2022	04:03	04:19	42.7	0.6
9	18-October-2022	06:16	02:20	45.8	0.3
10	20-October-2022	06:28	00:54	48.4	0.7
11	2022-October-2022	05:43	01:19	87.0	0.8
12	28-October-2022	06:12	01:02	41.8	0.6
13	30-October-2022	03:08	04:28	73.0	1.0
14	31-October-2022	05:43	00:27	209.3	0.4
15	12-November-2022	07:39	00:34	177.7	1.2
16	13-November-2022	00:34	08:41	112.9	1.1
17	17-November-2022	04:34	02:42	67.9	0.9
18	18-November-2022	03:08	01:48	107.3	0.3
19	24-November-2022	03:41	03:18	89.1	1.1
20	26-November-2022	06:28	00:17	127.6	0.4
21	29-November-2022	03:50	01:27	151.7	0.3
22	2-December-2022	23:36	03:35	167.4	1.5
23	9-December-2022	01:26	01:23	234.9	1.2
24	16-December-2022	03:41	02:59	128.1	0.5
25	22-December-2022	05:50	00:20	470.0	0.7
26	4-January-2023	07:22	00:28	223.0	1.4
27	6-February-2023	05:03	02:14	363.2	0.7

Note. Fog onset, duration, and associated minimum horizontal visibility (m) and average horizontal wind speed (m s^{-1}) at WISE-UAE location for each of the 27 fog events that occurred during the field campaign.

3.2. Diurnal Variability in Meteorological Variables at WISE-UAE Location

In this section, the intricate diurnal variability in surface layer parameters during Phase-1 of the WISE-UAE experiment is elucidated.

Figure 7 provides a comprehensive overview of key parameters such as air temperature and RH at a 2 m height, and wind speed at a 10-m height. Notably, a distinct shift in the timing of the daily maximum air temperature is evident as we progress from the summer months to autumn and subsequently, winter. The peak temperatures occur between 12 and 15 LT, placing it somewhere between the coastal location of Barakah, where the daily maximum temperature takes place around 11–12 LT (Nelli et al., 2022), and the inland location of Al Ain, where the highest temperatures normally occur around 16–17 LT (Nelli et al., 2020b). This difference in timing can be attributed to a stronger sea-breeze influence in the western and central regions of the UAE, as opposed to the eastern inland location of Al Ain (Eager et al., 2008; Nelli, Fissehaye, et al., 2021). The difference in daily maximum air temperature between summer and winter is roughly 22°C, a typical value in hyper arid locations

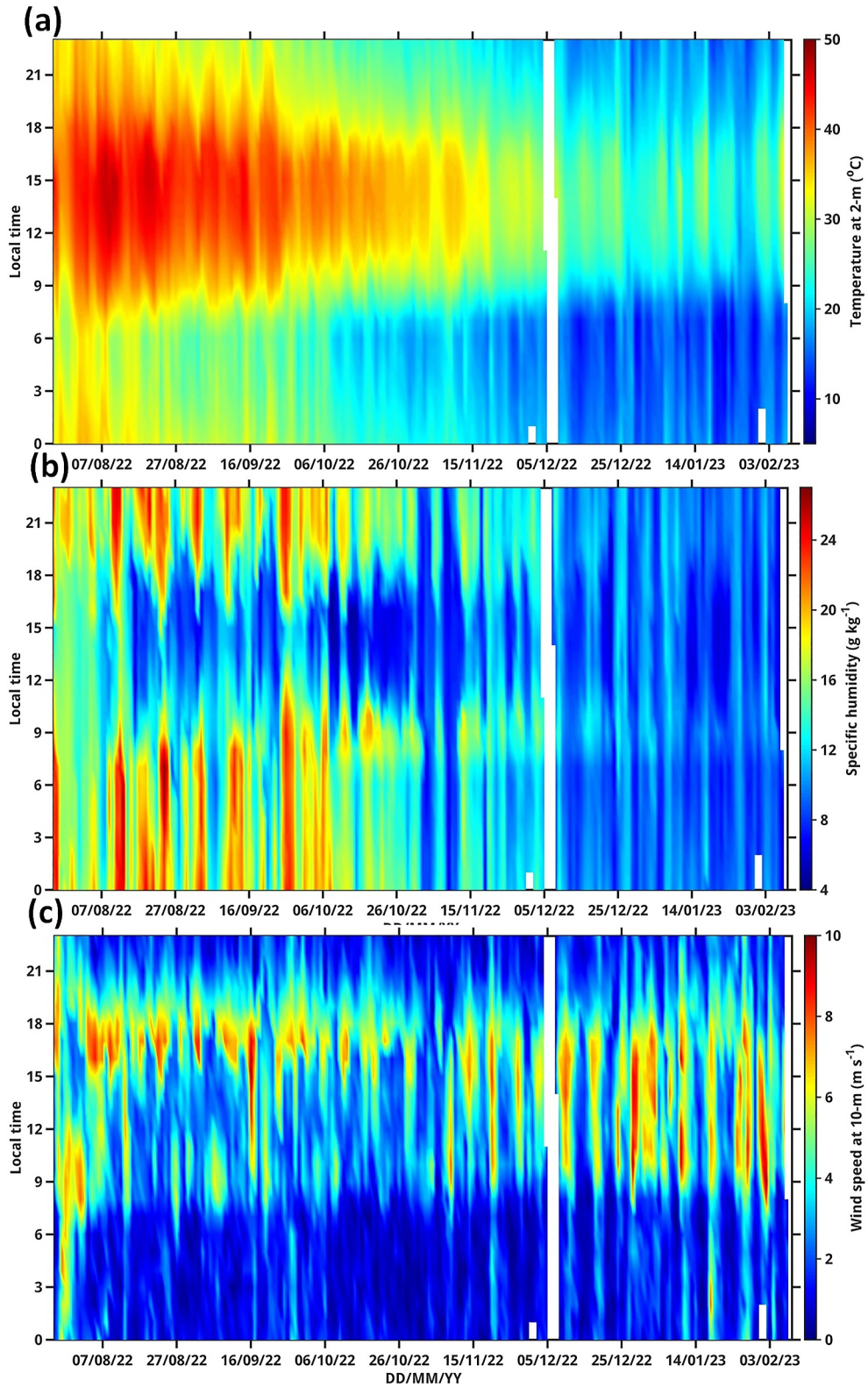

Figure 7. Diurnal Variability of meteorological fields at the WInd-blown Sand Experiment-United Arab Emirates location. Diurnal variability in hourly averaged (a, b) temperature (°C) and specific humidity (g kg^{-1}) at a 2 m height, and (c) wind speed (m s^{-1}) at 10 m height. The vertical axis indicates the time in local time (UTC + 4). The white gaps denote missing data.

(e.g., Rehman, 2010). These observations align well with those reported at other UAE locations (Branch et al., 2021; Nelli et al., 2020b, 2022).

The second panel in Figure 7 unveils the diurnal variability of specific humidity at the site. The increase in moisture in the warmer months, associated with the higher sea surface temperatures and therefore evaporation over the Arabian Gulf with the moist air transported inland by the large-scale flow and sea-breeze circulation, is seen in the plot. The commencement of the summer Shamal winds around May-June (Yu et al., 2016) facilitates the inland movement of humid marine air, thereby contributing to a steady increase in specific humidity. The lowest specific humidity values are typically registered in the cold season from December to February, often associated with the lower SSTs and advection of drier air from continental Asia (Nesterov et al., 2021). The primary moisture sources for the region have been identified as the Arabian Gulf, Red Sea, and Arabian Sea (Nelli et al., 2022; Taraphdar et al., 2021). The diurnal variations in specific humidity observed at the WISE-UAE location agree with those observed at other sites such as Barakah (Nelli et al., 2022) and Al Ain (Nelli et al., 2020b).

The third panel of Figure 7 shows the diurnal variability of the 10-m wind speed. As noted earlier, 10-m hourly averaged wind speeds at the WISE-UAE location were predominantly below 4 m s^{-1}. There are two broad and distinct peaks in wind speed - one around 9–10 LT and a second one roughly between 16 and 18 LT. Interestingly, during the transition months from summer to winter, a single extended period of maximum wind speed is observed. The diurnal maximum values are typically observed during the afternoon hours, corresponding to the latter peak, and are associated with the daytime sea-breeze circulation (Eager et al., 2008). The first peak during early morning hours, on the other hand, is triggered by a different mechanism. The nighttime low-level jet, a common feature of atmospheric dynamics in arid regions, is caused by the rapid cooling of the surface after sunset, resulting in the formation of a stable layer near the surface and a layer of stronger winds above. As the sun rises and the surface warms, the stability of the surface layer breaks down, causing the higher momentum air from above to be mixed downwards, which results in an increase in the surface wind speeds in the early morning (e.g., Bou Karam Francis et al., 2017; Giannakopoulou & Toumi, 2012; Nelli et al., 2020b, 2022). The extended peak in wind speed observed during the summer to winter transition months could result from the delay in nocturnal jet intrusion to the surface owing to longer nights, coupled with a shift in the timing of the peak sea-breeze circulation to earlier in the day. Similar variations have been observed by Nelli et al. (2020b) at the Al Ain location. These dynamics are complex and warrant further investigation, which extends beyond the scope of our current study.

Figures 8a and 8b presents the diurnal variations in the net shortwave (SW) and longwave (LW) radiation fluxes, offering key insights into the radiative transfer processes at our location. Figure 8c gives the daily averaged profile of soil temperatures at three levels, +5 cm, the skin, and −5 cm, during the initial phase of WISE-UAE. To the best of our knowledge, WISE-UAE is among the first long-term measurements of soil temperature in the region, following the ones by Nelli et al. (2020b) at Al Ain.

As anticipated, we observe a significant decline in the peak of the net SW radiation flux, by nearly 300 W m^{-2} or a third of its magnitude from the height of the summer months in July to December. This reduction can be primarily attributed to the decreasing solar zenith angle as the seasons transition from summer to winter. Such a downward trend is also present in the soil temperature, with the skin temperature ranging from a high of 44°C to a low of 16°C. This shift is representative of the dramatic seasonal changes experienced in this arid environment, and reflects the considerable heat storage capacity of the desert soil. Day-to-day variability is present and largely aligned with that in the meteorological fields shown in Figure 7: for example, from late December 2022 to early February 2023, there are days when the net SW radiation flux remained below 300 W m^{-2} throughout the whole day, which co-occurred with cooler air temperatures (cf. Figure 7a) and high RH values (cf. Figure 7b) and some with high wind speeds (cf. Figures 5 and 7c). These were cloudy days when the region was under the influence of mid-latitude low pressure systems, as noted by the IRBT data given in Figure 4. The less negative values of net LW radiation flux (Figure 8b) on these days are consistent with the higher cloud amounts which act to enhance the downward LW radiation flux. Reduced levels of net SW radiation flux are also observed in the warmer months, such as in mid-August 2022.

A comparison with Figures 7 and 8b indicates they are likely dusty days, given that (i) the RH remained below 40% throughout the day (Figure 7b); they featured warmer nighttime and cooler daytime temperatures by up to 5°C (Figure 7a) with respect to those observed in the neighboring days; (iii) the IRBT was typically higher than 270–280 K, indicating clear skies, while the visibility dropped at times below 1 km (Figure 4) and the wind speed

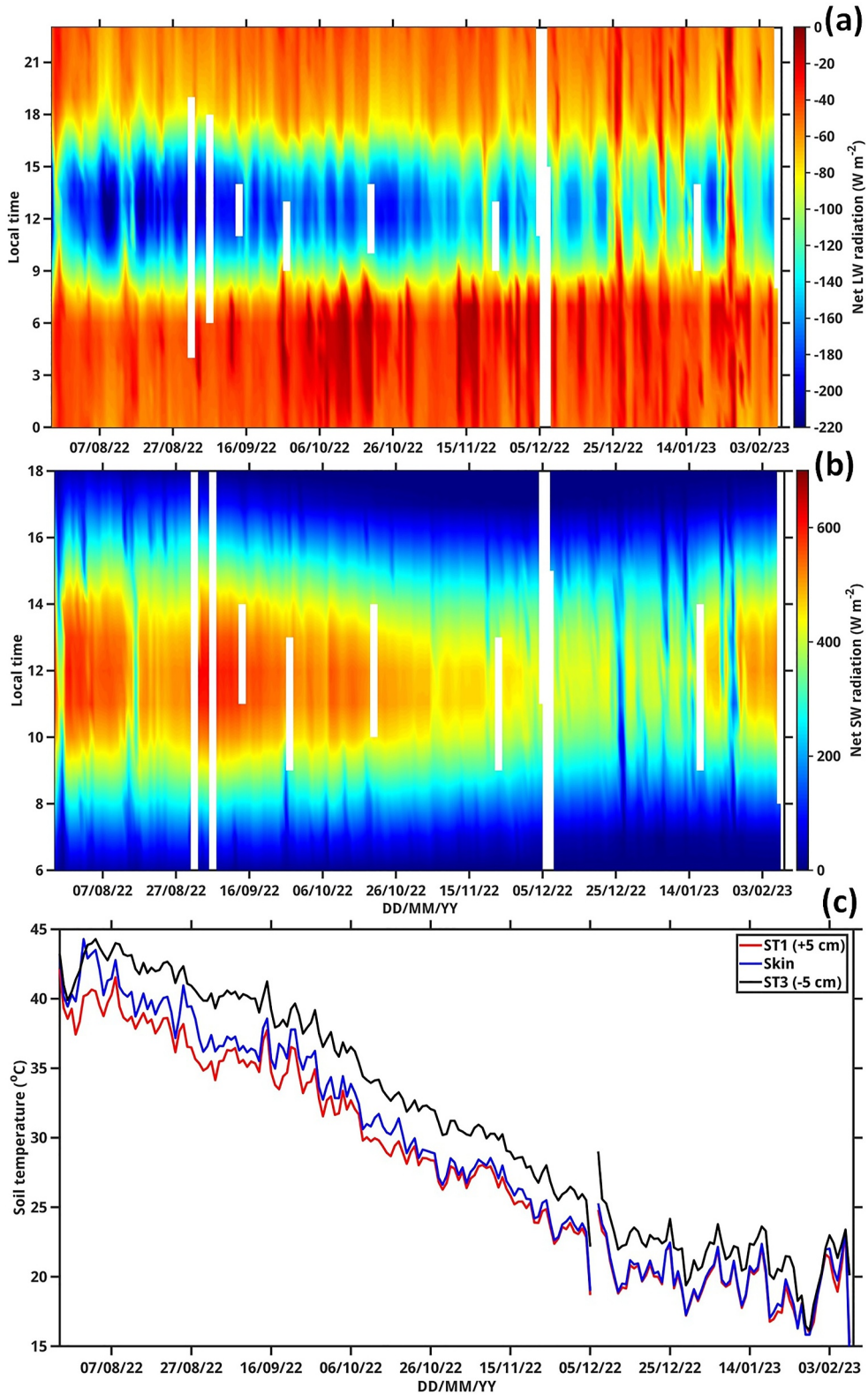

Figure 8. Diurnal variability of radiation and soil fields at the WInd-blown Sand Experiment-United Arab Emirates location. Day-to-day variability in the hourly averaged net shortwave (SW, a) and longwave (LW, b) radiation fluxes (W m^{-2}). The conventions are as in Figure 7. (c) Daily-averaged air temperature (°C) at +5 cm above the ground, skin or just above the surface, soil temperature at −5 cm below the ground.

was in excess of 5 m s^{-1} (Figure 5). Such changes in the near-surface atmospheric conditions have been observed for example, during the May 2022 dust storm in the country (Francis et al., 2023). The pattern of the diurnal variability in the surface net LW radiation flux largely follows that of the air temperature, with more negative values during daytime. This is expected, as the downward longwave radiation flux, largely controlled by the atmospheric emissivity and cloud cover, exhibits a reduced diurnal range when compared to the upward longwave radiation flux, which is essentially a function of the surface temperature that has a much more pronounced diurnal variability (Nelli et al., 2020b). The range of values for the net SW and LW radiation fluxes at the WISE-UAE site is similar to that observed at Al Ain in eastern UAE during a field campaign from April 2017 to January 2019 (Nelli et al., 2020b) and therefore are representative of those in the region. From the upward (SW↑) and downward (SW↓) SW radiation fluxes, the surface albedo, a critical parameter in determining the reflectivity of the surface and thus the amount of solar radiation absorbed or reflected, can be estimated as follows

$$\alpha = \frac{\mathrm{SW}\uparrow}{\mathrm{SW}\downarrow} \tag{1}$$

The average surface albedo at our WISE-UAE location is found to be 0.339 ± 0.020. This value is in line with the 0.334 estimated at Al Ain (Nelli et al., 2020b) and with those estimated in other desert regions (e.g., Cordero et al., 2021; Ryder et al., 2013). The relatively higher albedo at the WISE-UAE location compared to Al Ain could be due to differences in soil texture and soil moisture (Temimi, Fonseca, Nelli, Weston, et al., 2020).

As the soil is warmed by the SW radiation from the Sun, the daily maximum temperature during daytime decreases with depth and the minimum temperature at night increases with depth, with typical magnitudes of -9°C and +6°C from depths of 2–15 cm estimated at Al Ain (Nelli et al., 2020b). The daily-mean values in Figure 8c show an increase with the depth by up to 5°C with respect to the skin temperature, suggesting the soil effectively retains the daytime warmth during the overnight hours. The air and skin temperatures are very similar in the colder months, but in the warmer months can be up to 5°C cooler. This is expected, as the Sun's SW radiation first heats the surface, with the atmosphere subsequently warmed up through sensible heat fluxes. On cloudy days during December 2022–February 2023 the changes in temperature from a height of +5 cm to −5 cm above the surface are much reduced and can even be negligible, in line with the lower amounts of SW radiation flux (cf. Figure 8a).

3.3. Aerodynamic and Thermal Roughness Lengths

To accurately assess the surface transportation of momentum, heat, and moisture, it's essential to utilize the M-O theory alongside the similarity principles given by Dyer and Hicks (1970) and Businger et al. (1971). These methods have been integrated into various climate and weather prediction models (Dudhia & Bresch, 2002; Rao & Reddy, 2019). A pivotal aspect of this application lies in adequately defining the aerodynamic and thermal roughness lengths. However, assigning accurate roughness lengths in numerical weather prediction models is difficult due to the varied nature of land surfaces and topography. For instance, the commonly utilized WRF model incorporates default parameters related to land use, such as roughness length, designated to specific categories of land surface and terrain types (Temimi, Fonseca, Nelli, Weston, et al., 2020). Determining the roughness lengths for individual land forms typically relies on field observations specific to that terrain (Nelli et al., 2020a; Reddy & Rao, 2016). In the present study, the aerodynamic roughness length (z_o) and the thermal roughness length (z_h) are estimated for the WISE-UAE location characterized by homogeneous terrain in a hyper-arid environment. Site-specific aerodynamic and thermal roughness lengths are derived under high wind and neutral conditions because the wind speed and temperature profiles in the surface layer adhere to logarithmic variations under these conditions (Rao & Reddy, 2019; Reddy & Rao, 2016). The parameter z_o represents the elevation above the ground where the average wind speed becomes null. It is typically determined by extending the logarithmic wind speed profile across various elevations until the point where the average wind speed ceases (Reddy & Rao, 2016). z_h denotes the elevation above the ground where the extrapolated logarithmic curve of air temperature variations, relative to the skin temperature, meets the zero point (Reddy & Rao, 2016). At the WISE-UAE location, measurements of skin and air temperatures are gathered from six distinct elevations using a 10-m high tower. Using the method outlined by Reddy and Rao (2016), the values for z_o and z_h are determined in conditions of high wind and near-neutral stability. The surface layer's static stability is examined through the bulk Richardson number, $\mathrm{Ri_B}$, as determined by

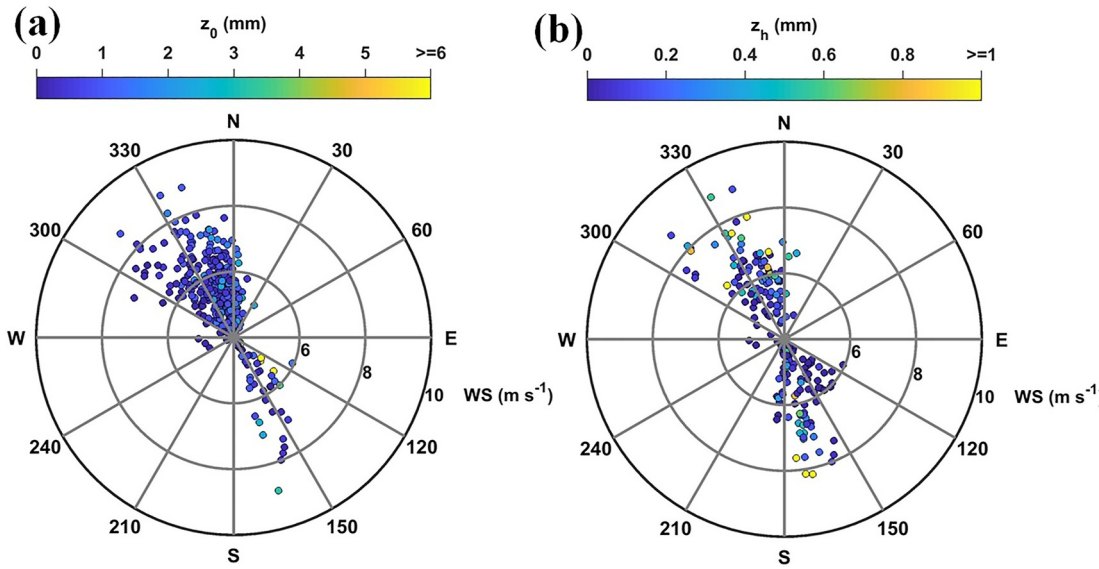

Figure 9. Aerodynamic and thermal roughness length at WInd-blown Sand Experiment-United Arab Emirates site. Variability in the (a) aerodynamic roughness length (z_o, mm) and (b) thermal roughness length (z_h, mm). The circles on the map indicate wind speed (m s^{-1}), while the colorbar represents the roughness length. The center of the circle denotes the wind speed of 4 m s^{-1}, increasing by 2 m s^{-1} from one circle to the next.

$$Ri_B = \left(\frac{g}{\theta}\right)\frac{\left(\frac{\Delta\theta}{\Delta z}\right)}{\left(\frac{\Delta U}{\Delta z}\right)^2} \quad (2)$$

where g is the gravitational acceleration, θ is the potential temperature, U is the wind speed and z is the height above the surface. The values of z_o and z_h are estimated for hourly wind speeds at a height of $z = 4$ m with $U > 4$ m s^{-1} and with Ri_B values in the range of −0.1 to +0.1, corresponding to near-neutral stability (Reddy & Rao, 2016). A total of 610 data points satisfied the high wind, near-neutral conditions. Among these, data points with R^2 values greater than 0.95 for the best fits between the wind speed and height for z_o and the temperature deviations and height for z_h are considered. After applying these criteria, a total number of 437 data points are used for estimating z_o and 201 data points are used to compute z_h.

Figures 9a and 9b show the variations in the aerodynamic and thermal roughness lengths. The majority of high wind near-neutral points fall into two wind sectors, 300°–0° and 200°–120°, respectively. The ranges of z_o in these two directions are 0.009–3.9 mm and 0.047–58.7 mm, respectively. The z_o values in the southwest direction, especially in the southern direction, are higher than those in the north west direction, by up to an order of magnitude. This is consistent with rougher terrain south of the site, and stresses the important role played by the land cover and topography in the magnitude of z_o. The average aerodynamic roughness lengths for two directions (N-NW and S-SE) are 0.9 ± 0.7 and 3.5 ± 10.4 mm, respectively. The sensitivity of z_0 to the RiB, wind speed and wind direction is shown in Figure S1–S4 in Supporting Information S1. Histograms of roughness lengths for different range bins are given in Figure S5 in Supporting Information S1. From Figure 9a and Figure S1–S4 in Supporting Information S1, it is noted that the higher standard deviation in z_0 values corresponds to the transition wind regime (i.e., high wind speed to strong wind speed, 4–6 m s^{-1}). To derive the site specific z_0 value, the z_0 values for strong wind speed in maximum prevailing wind direction are considered. The average z_o value for strong wind conditions (>6 m s^{-1}) and for the maximum prevailing wind directions is 0.8 ± 0.6 mm, obtained for the WISE-UAE location (homogeneous bare-soil). This estimate is consistent with that reported for a homogeneous hyper-arid land surface at Al Ain, UAE (Nelli et al., 2020a), indicating that the results of this study are robust and can be compared with other measurements conducted in similar environments.

The average thermal roughness lengths for two directions (N-NW and S-SE) are 0.3 ± 0.4 and 0.2 ± 0.3 mm, respectively. The average z_h value, for strong wind conditions (>6 m s^{-1}) and for the maximum prevailing wind directions is 0.3 ± 0.5 mm, which agrees with K. Yang et al. (2008). The ratio z_o/z_h is a crucial parameter

influencing the comparative effects of surface roughness on the air flow movement and heat exchange. For the WISE-UAE location, the ratio z_o/z_h is 3 and 17.5 for two dominant prevailing wind directions (NW and SE), respectively. These values are consistent with those reported for bare-soil surfaces by K. Yang et al. (2008). The estimation of the parameter kB^{-1}, defined as $\ln(z_o/z_h)$ using turbulence parameters, falls outside the scope of this study and will be presented elsewhere.

3.4. Threshold Wind Speed for Saltation Occurrence

This section focuses on characterizing saltation by studying its diurnal variations and determining the threshold wind speed necessary for its occurrence. During the WISE-UAE experiment, saltation was measured using both the Eijkelkamp and Wenglor sensors. Throughout the study period, we recorded a substantial number of saltation events, each with varying duration and intensity. The Eijkelkamp sensor recorded saltation counts across all prevailing wind directions. In contrast, the Wenglor sensor, being an optical-type instrument, was set to capture data only in the NW-SW direction. Although the Wenglor sensor provides accurate detection of saltation events, its direction is fixed in this study. For a comprehensive understanding of saltation across the most prevailing wind directions, we first compared data from the Eijkelkamp (often referred to as the saltiphone) and the Wenglor sensors. This comparison is for three specific saltation events that occurred on 30 September, 9 November 2022, and 7 February 2023 (Figure 10a). After this comparative analysis, we utilized the Eijkelkamp sensor data to understand saltation frequency across different months, its diurnal variations, and importantly, the threshold wind speed at which saltation initiates.

Following Sow et al. (2009), we excluded saltation counts below 100 and those related to low wind speeds at 10-m height (<4 m s^{-1}, Nelli et al., 2022; Rao & Reddy, 2019). In analyzing Saltiphone data, we observed recordings influenced by fog droplet deposition during conditions of low wind, high humidity, and fog. To ensure accuracy, we excluded measurements at wind speeds below 4 m s^{-1}, effectively filtering out these affected data points. Furthermore, as depicted in both hourly averaged winds (Figure 5) and one-minute resolution data (Figure S6 in Supporting Information S1), it is evident that high wind occurrences outside the primary wind sectors (280°–50°, S1 to S2 in Figure 1b) account for less than 1% of events. Therefore, we have focused our analysis exclusively on events occurring within this primary wind sector. Figure 10a describes the saltation counts (expressed in counts/minute) captured by both the Eijkelkamp and Wenglor sensors during the three saltation events. It is evident that the counts from the Eijkelkamp sensor closely agree with periods of high wind conditions and consistently match the readings from the Wenglor sensor, particularly for north-northwest winds (Figure S7 in Supporting Information S1). The correlation coefficient between two saltation sensors saltation counts in the Wenglor alignment direction (N-NW and S-SE) 0.35, significant at 99% confidence level. This small positive correlation may result from the sensors not being calibrated against a common reference and the potential lead-lag in the data from the two sensors. To characterize saltation and to derive the threshold wind speed for the WISE location, we primarily relied on data from the Eijkelkamp sensor. It is important to mention that the Eijkelkamp sensor began its operation on 18 September 2022. Between 18 September 2022 and 8 February 2023, a total of 38 days exhibited saltation events. The monthly breakdown is as follows: September (3 days), October (3 days), November (4 days), December (11 days), January (14 days), and February (3 days).

Figure 10b illustrates the diurnal frequency of saltation events. At the WISE location, our findings indicate that saltation primarily takes place during daytime hours, specifically from 08:00 to 18:00 LT. The peak activity is notably concentrated between 11:00 and 15:00 LT (Figure 10b). Similar findings for the timing of saltation occurrence have been reported for other deserts such as the Llano Estacado (Stout & Arimoto, 2010), the Taklimakan Desert (X. H. Yang et al., 2013), the Bodele depression in Africa (Todd et al., 2008), and the White Sand Dune Field in New Mexico (Gunn et al., 2021). To gain insight on the drivers for this diurnal cycle, we present in Figure 10c a composite of 10-m wind speeds for all the days with observed saltation. A maximum surface wind speed is observed between 10:00 and 18:00 LT coinciding with the highest frequency of saltation discussed earlier. The surge in morning surface wind speed results from the downward momentum transfer originating from the nighttime low-level jet (e.g., Bou Karam Francis et al., 2017; Francis, Fonseca, et al., 2022; Nelli et al., 2022; Washington & Todd, 2005). An additional increase in surface wind speed during saltation days is observed around 15 LT and is associated with the sea breeze circulation.

At sunrise, the air temperature begins to rise, reaching its daily peak around 15:20 LT (Figure 7a). This increasing air temperature leads to the growth of the mixed layer, which also reaches its maximum depth in the early

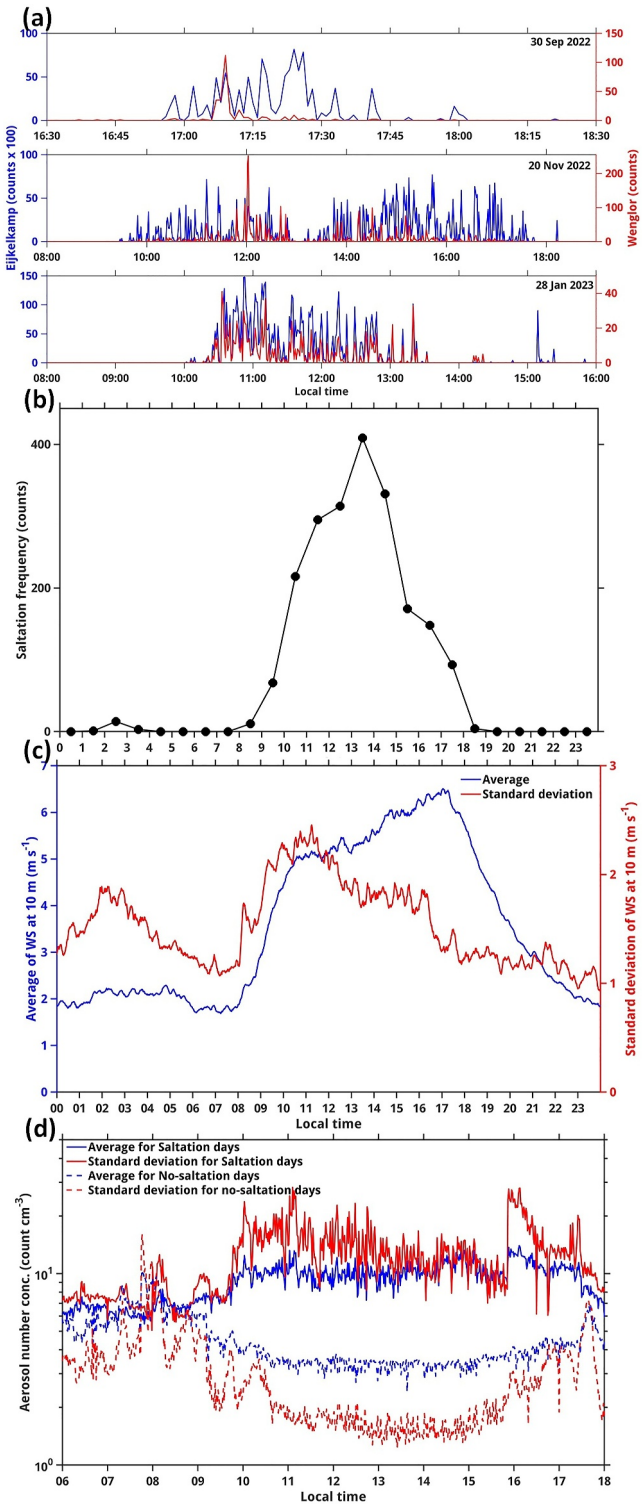

Figure 10. Occurrence of saltation at WInd-blown Sand Experiment location. (a) Saltation counts obtained from Eijkelkamp and Wenglor sensors during typical events on 30 September and 9 November 2022, as well as 7 February 2023. (b) Diurnal variation of saltation frequency for 38 saltation days. (c) Diurnal composite of wind speed at 10 m across the 38 saltation days. (d) Composite of aerosol number concentration at 2-m height for 38 saltation (solid lines; counts cm^{-3}) and 15 no-saltation days (dashed lines). Blue (red) solid line in (c, d) indicates the average (standard deviation).

afternoon hours coinciding with the daily temperature peak (Filioglou et al., 2020; Kesti et al., 2022). The dust particle concentration near the surface is influenced by the strength of the mixed layer. As such, it exhibits its lowest concentration around the time of maximum air temperature and mixed layer height. In contrast, during the transitions between the convective and stable boundary layers (and vice versa), the dust particle concentration near the surface spikes. This increase can be attributed to the atmosphere's propensity during these transition periods to accumulate dust, leading to elevated dust particle concentrations (Jin & He, 2023).

In this study, we sought to explore the variability in particle concentrations during both saltation and no-saltation days. No-saltation days are those when the saltation counts from both the Saltiphone and Wenglor sensors are zero. During phase-1 of WISE-UAE, 15 no-saltation days were observed. The composite of particle number concentrations, ranging from 0.3 to 20 μm, for these no-saltation days is presented in Figure 10d as dashed lines. As previously noted, the particle concentrations are at their lowest during afternoon hours, a period that also corresponds with peak SW radiation flux and elevated air temperatures (Figure 8a). Conversely, the particle concentrations on saltation days are notably higher (by roughly 1.7 times, as indicated by the solid line in Figure 10d). This surge can be attributed to local dust particle emissions resulting from saltation events (Figure 10b).

Saltation only transpires when the wind speed crosses a certain threshold. Literature cites various threshold values for different regions: 6.7 ± 1.5 m s^{-1} for the Taklimakan Desert, 9.4 ± 1.6 m s^{-1} for the Loess Plateau, 13.8 ± 2.0 m s^{-1} for the Gobi Desert, 12.3 ± 0.9 m s^{-1} for northeastern China, 9.7 ± 1.4 m s^{-1} for the North China Plain, 16.2 ± 2.5 m s^{-1} for northern Mongolia, and 10.5 m s^{-1} for the Chihuahuan Desert sites in the Mescalero Sands, east of Carlsbad, New Mexico (Kurosaki & Mikami, 2007; Stout & Arimoto, 2010). Chomette et al. (1999) utilized the Infrared Difference Dust Index in conjunction with European Center for Medium-Range Weather Forecasts (ECMWF) reanalysis 10 m wind between 1990 and 1992. They determined the wind threshold for dust emission over seven sites across the Sahel and Sahara. The average wind erosion threshold varied, ranging from 6.63 m s^{-1} at a site in the Sahel to approximately 9.08 m s^{-1} at a site in Niger (Table 1 of Chomette et al., 1999). These threshold values can vary due to multiple factors, such as atmospheric conditions and the characteristics of the soil surface. These factors include air temperature, humidity, soil particle size, moisture level, vegetation, and other conditions (X. Yang et al., 2018 and associated references). Given these variations, the threshold wind speed for saltation is inherently location-specific. In this context, we endeavored to derive the threshold wind speed specifically for the Empty Quarter Desert using data from the WISE-UAE measurements.

In our current study for the WISE-UAE location, we employed a static method to determine this threshold. This method has been proposed and utilized in previous studies, including those by Park and In (2003), Kurosaki and Mikami (2007), and X. Yang et al. (2018). The method is based on the following equation:

$$f_{\mathrm{sal}|u} = \frac{N_{\mathrm{sal}|u}}{N_{\mathrm{all}|u}} \times 100\% \tag{3}$$

where $f_{\mathrm{sal}|u}$ represents the percentage of saltation occurrence for each wind speed bin, $N_{\mathrm{sal}|u}$ denotes the number of saltation occurrences within each wind speed bin, and $N_{\mathrm{all}|u}$ is the total count for each wind speed bin. Wind speeds are binned in 0.2 m s^{-1} intervals. The threshold wind speed is defined as the speed where saltation occurs 50% of the time. Note that while this statistical approach accounts for variability in meteorological variables and soil properties, it yields only the long-term median value and does not provide time-dependent threshold wind speeds. Using this approach, we derived a threshold wind speed of 7.70 m s^{-1} for the WISE location (Figure 11). This finding aligns closely with the 7 m s^{-1} threshold often linked to dust activity in the Middle East, as mentioned by Yu et al. (2016). It's worth noting that our derived threshold wind speed for saltation, which is higher than the frequently assumed constant threshold wind speed of 6.5 m s^{-1} in various models, challenges some existing assumptions (e.g., Uno et al., 2001). We adopted a methodology similar to that used for wind speed measurements at a height of 10 m, but instead focused on wind speed measurements at 0.4 and 2.25 m above the ground. We determined that the threshold wind speeds required for saltation occurrence at these respective heights are 5.67 and 6.71 m s^{-1}.

Our comprehensive analysis, leveraging both the Eijkelkamp and Wenglor sensors, has provided valuable insights into the intricate dynamics of saltation events in the UAE. The derived threshold values, grounded in

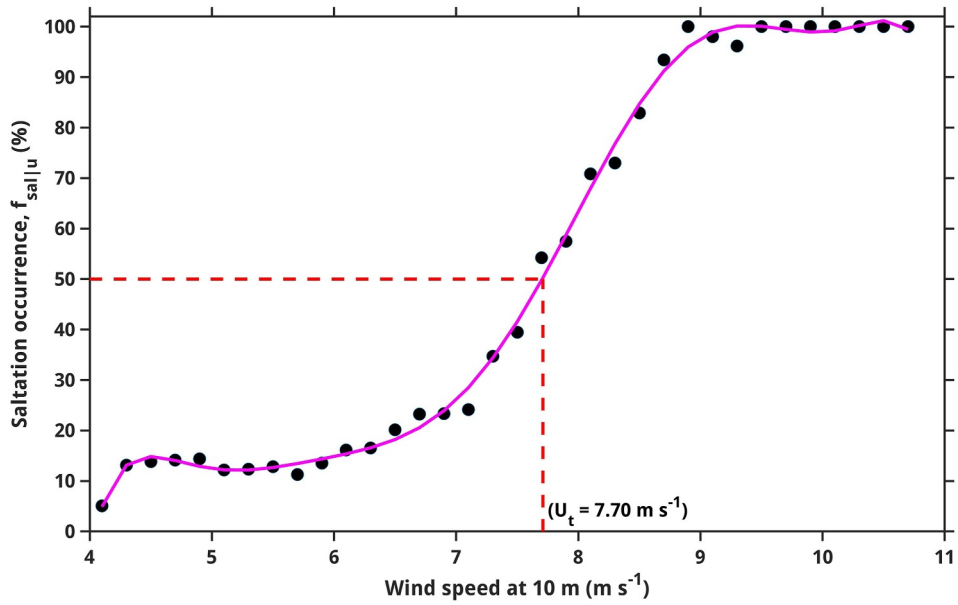

Figure 11. Threshold wind speed for saltation occurrence. The solid purple line indicates the best-fit curve for the bin-averaged saltation occurrence values. Wind speeds are binned in 0.2 m s^{-1} intervals.

rigorous methodology, not only contribute to the broader understanding of aeolian processes but also highlight the subtle interplay of atmospheric and terrestrial conditions in shaping regional dust phenomena.

4. Summary

In this paper, we present new insights on the dynamics of the Empty Quarter Desert environment derived from in-situ measurements acquired during the WISE-UAE campaign, a first-of-its-kind in the region. These included measurements of multiple environmental variables such as saltation, wind patterns, temperature, humidity, radiation fluxes, atmospheric electric field, and soil properties.

At the WISE-UAE location, the wind predominantly blows from three directions: northwesterly (280°–320°, sector-1), northeasterly (20°–50°, sector-2), and south-southwest to easterly (210°–100°, sector-3). The area features a flat topography, extending over 300 m in the maximum prevailing wind direction (sector-1). Vegetation is sparse, with only small bushes present to the east of the site, and a national highway is situated approximately 300 m east of the monitoring tower. The solar plant is situated approximately 110 m southwest of our measurement site, in the non-prevailing wind direction. The site is characterized by a loamy sand soil type, which is highly susceptible to wind erosion. Throughout the campaign we observed a variety of meteorological conditions, including convective conditions, dust storms, Shamal events, and foggy days.

The average wind speed measured at 10-m height during the WISE-UAE campaign was 2.8 ± 1.9 m s^{-1}, with the occurrence of low wind speed (<4 m s^{-1}) found to be 76.4%. Its diurnal variability is dominated by mesoscale circulations, such as the sea-land breeze circulation, and by the downward momentum mixing from the nighttime low-level jet in early morning hours. We quantify the effect of the surface features on the wind flow by estimating the aerodynamic roughness length (z_0) under high wind near-neutral conditions. The average z_0 obtained for the WISE-UAE site, which features a homogeneous bare-soil landscape, is 0.8 ± 0.6 mm. This estimate is in line with previously reported values for a similar hyper-arid land surface at Al Ain, UAE (Nelli et al., 2020a).

Furthermore, we estimated the thermal roughness length (z_h), marking the first estimation of this kind for any location in the UAE. The average z_h at the WISE-UAE site is 0.3 ± 0.5 mm, corroborating the findings of K. Yang et al. (2008). The ratio of z_o/z_h varied substantially with wind direction, amounting to 3 and 17.5 for the dominant prevailing wind directions northwest and southeast, respectively. This variation in ratio under different wind conditions provides valuable insights into the dynamic interaction between the wind and the bare soil surface. Additionally, the values of z_0 and z_h are pivotal for understanding soil erosion, dust emission, and deposition

processes. These measurements are not only essential for meteorological modeling but also useful for agricultural planning and infrastructure development in hyper-arid regions. The surface albedo is estimated to be 0.339 ± 0.020, and is in line with the values reported at other desert sites (Cordero et al., 2021; Nelli et al., 2020b). The daily-mean soil temperature at 5 cm depth is generally higher than that surface skin temperature by up to 5°C, although on cloudy and cooler days in the colder months the two can have comparable values.

The comprehensive analysis of saltation events between 18 September 2022 and 8 February 2023, using the Eijkelkamp sensor, recorded a total of 38 days with saltation occurrence. The diurnal frequency indicated a primary activity peak between 13:00 and 14:00 LT. An examination of the variability in the near-surface particle concentration during saltation and no-saltation days revealed that particle concentrations were 1.78 times higher during saltation days. The derived threshold wind speeds for saltation varies across regions, with our study identifying a threshold wind speed of 7.70 m s^{-1} for the Empty Quarter in the UAE. The established threshold wind speed for saltation is crucial for predicting sand movement and informs both regional planning and mitigation strategies against dust storms. This finding is instrumental in developing more accurate models for desert dynamics and dust transport, which are vital for climate research and the management of local ecosystems.

Building on the current results, the campaign will continue investigating the desert environmental dynamics with specific focus on the variability in the atmospheric electric field under foggy and dusty conditions, atmospheric and soil interactions, wind speed's influence on dust aerosol emission, the soil moisture's impact on wind erosion and the radiative impacts of dust aerosols. All of which will be covered in future work.

These explorations will not only augment our knowledge about the complex dynamics of desert environments but can also support the development of more accurate weather and climate models for arid regions. The data produced during this campaign offers a valuable resource for validating satellite and reanalysis products as well as model forecasts.

Conflict of Interest

The authors declare no conflicts of interest relevant to this study.

Data Availability Statement

The data files used in this paper are available at (Nelli, 2023). The Satellite and reanalysis data sets used in this work are freely available online. They include the (a) false color satellite images generated from the measurements collected by the Spinning Enhanced Visible and Infrared Imager (SEVIRI) instrument are available on the European Organization for the Exploitation of Meteorological Satellites' website (EUMETSAT, 2017); (b) ERA-5 reanalysis data can be downloaded from the Copernicus' Climate Change Service website (Hersbach et al., 2018a, 2018b, 2019a, 2019b). All figures were generated using the Interactive Data Language (IDL) software version 8.8.1 and Matlab (MATLAB, 2021) software release 2021b (R2021b).

Acknowledgments
The authors extend their gratitude to Khalifa University for the invaluable support provided by its high-performance and research computing facilities, which significantly contributed to this research's outcomes. Our sincere thanks also go to the SHAMS solar power company (https://www.shamspower.ae/) and Emirates Tech (ETECH; https://www.etechuae.com/) for their critical assistance and cooperation during the WISE-UAE field campaign. This research endeavor was generously sponsored by the Federal Authority for Nuclear Regulation (FANR) as a part of the research initiative titled Modeling of Radionuclides Dispersion in the UAE Environment (MORAD). We are also grateful to the French Radioprotection and Nuclear Safety Institute (IRSN) for providing aerosol analyzers, analyzers sample heads, the Wenglor salation sensor, and the Modified Wilson and Cooke (MWAC) sand traps. It is with great gratitude that we thank Amel Kort and Pauline Wiszniowski from the IRSN for kindly providing aerosol analyzer calibration reports. We would also like to express our gratitude to the two anonymous reviewers for their constructive and insightful comments, which have significantly contributed to enhancing the quality of this work.

References

Abida, R., Addad, Y., Francis, D., Temimi, M., Nelli, N., Fonseca, R., et al. (2022). Evaluation of the performance of the WRF model in a hyper-arid environment: A sensitivity study. *Atmosphere*, *13*(6), 985. https://doi.org/10.3390/atmos13060985

Alfaro, S. C., Gaudichet, A., Gomes, L., & Maillé, M. (1998). Mineral aerosol production by wind erosion: Aerosol particle sizes and binding energies. *Geophysical Research Letters*, *25*(7), 991–994. https://doi.org/10.1029/98GL00502

Al-Hemoud, A., Al-Dashti, H., Al-Saleh, A., Petrov, P., Malek, M., Elhamoud, E., et al. (2022). Dust storm 'hot spots' and transport pathways affecting the Arabian Peninsula. *Journal of Atmospheric and Solar-Terrestrial Physics*, *238–239*, 105932. https://doi.org/10.1016/j.jastp.2022.105932

Al Senafi, F., & Anis, A. (2015). Shamals and climate variability in the northern Arabian/Persian Gulf from 1973 to 2012. *International Journal of Climatology*, *35*(15), 4509–4528. https://doi.org/10.1002/joc.4302

Bagnold, R. A. (1941). *The physics of blown sand and desert dunes* (p. 265). Methuen.

Barchyn, T. E., & Hugenholtz, C. H. (2010). Field comparison of four piezoelectric sensors for detecting aeolian sediment transport. *Geomorphology*, *120*(3–4), 368–371. https://doi.org/10.1016/j.geomorph.2010.03.034

Barchyn, T. E., Hugenholtz, C. H., Li, B., McKenna Neuman, C., & Sanderson, R. S. (2014). From particle counts to flux: Wind tunnel testing and calibration of the 'Wenglor' aeolian sediment transport sensor. *Aeolian Research*, *15*, 311–318. https://doi.org/10.1016/j.aeolia.2014.06.009

Basha, G., Ratnam, M. V., Niranjan Kumar, K., Ouarda, T. B. M. J., Kishore, P., & Velicogna, I. (2019). Long-term variation of dust episodes over the United Arab Emirates. *Journal of Atmospheric and Solar-Terrestrial Physics*, *187*, 33–39. https://doi.org/10.1016/j.jastp.2019.03.006

Bauer, B. O., Davidson-Arnott, R. G. D., Hilton, M. J., & Fraser, D. (2018). On the frequency response of a Wenglor particle-counting system for aeolian transport measurements. *Aeolian Research*, *32*, 133–140. https://doi.org/10.1016/j.aeolia.2018.02.008

Bou Karam Francis, D., Flamant, C., Chaboureau, J.-P., Banks, J., Cuesta, J., Brindley, H., & Oolman, L. (2017). Dust emission and transport over Iraq associated with the summer Shamal winds. *Aeolian Research*, *24*, 15–31. https://doi.org/10.1016/j.aeolia.2016.11.001

Branch, O., Schwitalla, T., Temimi, M., Fonseca, R., Nelli, N., Weston, M., et al. (2021). Seasonal and diurnal performance of daily forecasts with WRF V3.8.1 over the United Arab Emirates. *Geoscientific Model Development*, *14*(3), 1615–1637. https://doi.org/10.5194/gmd-14-1615-2021

Businger, J. A., Wyngaard, J. C., Izumi, Y., & Bradley, E. F. (1971). Flux–profile relationships in the atmospheric surface layer. *Journal of the Atmospheric Sciences*, *28*(2), 181–189. https://doi.org/10.1175/1520-0469(1971)028<0181:FPRITA>2.0.CO;2

Chepil, W. S. (1951). Properties of soil which influence wind erosion: IV. State or dry aggregate structure. *Soil Science*, *72*, 387–401.

Chomette, O., Legrand, M., & Marticorena, B. (1999). Determination of the wind speed threshold for the emission of desert dust using satellite remote sensing in the thermal infrared. *Journal of Geophysical Research*, *104*, 31207–31215. https://doi.org/10.1029/1999JD900756

Cordero, R. R., Feron, S., Sepulveda, E., Damiani, A., Carrera, J. M., Jorquera, J., et al. (2021). Evaluation of MODIS-derived estimates of the albedo over the Atacama Desert using ground-based spectral measurements. *Scientific Reports*, *11*(1), 19822. https://doi.org/10.1038/s41598-021-98622-4

Davidson-Arnott, R. G. D., Bauer, B. O., Walker, I. J., Hesp, P. A., Ollerhead, J., & Delgado-Fernandez, I. (2009). Instantaneous and mean aeolian sediment transport rate on beaches: An intercomparison of measurements from two sensor types. *Journal of Coastal Research*, *56*, 297–301. Retrieved from https://www.jstor.org/stable/25737585

Dudhia, J., & Bresch, J. F. (2002). A global version of the PSU-NCAR mesoscale model. *Monthly Weather Review*, *130*(12), 2989–3007. https://doi.org/10.1175/1520-0493(2002)130<2989:AGVOTP>2.0.CO;2

Dupont, S., Rajot, J.-L., Lamaud, E., Bergametti, G., Labiadh, M., Khalfallah, B., et al. (2021). Comparison between eddy-covariance and flux-gradient size-resolved dust fluxes during wind erosion events. *Journal of Geophysical Research: Atmospheres*, *126*(13), e2021JD034735. https://doi.org/10.1029/2021JD034735

Dyer, A. J., & Hicks, B. B. (1970). Flux-gradient relationships in the constant flux layer. *Quarterly Journal of the Royal Meteorological Society*, *96*(410), 715–721. https://doi.org/10.1002/qj.49709641012

Eager, R. E., Raman, S., Wootten, A., Westphal, D. L., Reid, J. S., & Al Mandoos, A. (2008). A climatological study of the sea and land breezes in the Arabian Gulf region. *Journal of Geophysical Research*, *113*(D15), D15106. https://doi.org/10.1029/2007JD009710

Esposito, F., Molinaro, R., Popa, C. I., Molfese, C., Cozzolino, F., Marty, L., et al. (2016). The role of the atmospheric electric field in the dust-lifting process. *Geophysical Research Letters*, *43*(10), 5501–5508. https://doi.org/10.1002/2016gl068463

EUMETSAT (European Organisation for the Exploitation of Meteorological Satellites). (2017). High rate SEVIRI level 1.5 image data—MSG—Indian Ocean 41.5 degrees E [Dataset]. *EUMETSAT*. Retrieved from https://navigator.eumetsat.int/product/EO:EUM:DAT:MSG:HRSEVIRI-IODC

Fécan, F., Marticorena, B., & Bergametti, G. (1999). Soil-derived dust emissions from semi-arid lands: 1. Parameterization of the soils moisture effect on the threshold wind friction velocities. *Annales Geophysicae*, *17*, 149–157. https://doi.org/10.1007/s00585-999-0149-7

Filioglou, M., Giannakaki, E., Backman, J., Kesti, J., Hirsikko, A., Engelmann, R., et al. (2020). Optical and geometrical aerosol particle properties over the United Arab Emirates. *Atmospheric Chemistry and Physics*, *20*(14), 8909–8922. https://doi.org/10.5194/acp-20-8909-2020

Fonseca, R., Francis, D., Nelli, N., & Cherif, C. (2023). Regional atmospheric circulation patterns driving consecutive fog events in the United Arab Emirates. *Atmospheric Research*, *282*, 106506. https://doi.org/10.1016/j.atmosres.2022.106506

Fonseca, R., Francis, D., Nelli, N., & Thota, M. (2022). Climatology of the heat low and the intertropical discontinuity in the Arabian Peninsula. *International Journal of Climatology*, *42*(2), 1092–1117. https://doi.org/10.1002/joc.7291

Fonseca, R., Francis, D., Weston, M., Nelli, N., Farah, S., Wehbe, Y., et al. (2021). Sensitivity of summertime convection to aerosol loading and properties in the United Arab Emirates. *Atmosphere*, *12*(12), 1687. https://doi.org/10.3390/atmos12121687

Francis, D., Chaboureau, J.-P., Nelli, N., Cuesta, J., Alshamsi, N., Temimi, M., et al. (2021). Summertime dust storms over the Arabian Peninsula and impacts on radiation, circulation, cloud development and rain. *Atmospheric Research*, *250*, 105364. https://doi.org/10.1016/j.atmosres.2020.105364

Francis, D., Fonseca, R., & Nelli, N. (2022). Key factors modulating the threat of the Arabian Sea's tropical cyclones to the Gulf countries. *Journal of Geophysical Research: Atmospheres*, *127*(12), e2022JD036528. https://doi.org/10.1029/2022JD036528

Francis, D., Fonseca, R., Nelli, N., Bozkurt, D., Cuesta, J., & Bosc, E. (2023). On the Middle East's severe dust storms in spring 2022: Triggers and impacts. *Atmospheric Environment*, *296*, 119539. https://doi.org/10.1016/j.atmosenv.2022.119539

Francis, D., Fonseca, R., Nelli, N., Teixido, O., Mohamed, R., & Perry, R. (2022). Increased Shamal winds and dust activity over the Arabian Peninsula during the COVID-19 lockdown period in 2020. *Aeolian Research*, *55*, 100786. https://doi.org/10.1016/j.aeolia.2022.100786

Francis, D., Nelli, N., Fonseca, R., Weston, M., Flamant, C., & Cherif, C. (2022). The dust load and radiative impact associated with the June 2020 historical Saharan dust storm. *Atmospheric Environment*, *268*, 118808. https://doi.org/10.1016/j.atmosenv.2021.118808

Giannakopoulou, E. M., & Toumi, R. (2012). The Persian Gulf summertime low-level jet over sloping terrain. *Quarterly Journal of the Royal Meteorological Society*, *138*(662), 145–157. https://doi.org/10.1002/qj.901

Gillette, D. A., Niemeyer, T. C., & Helm, P. J. (2001). Supply-limited horizontal sand drift at an ephemerally crusted, unvegetated saline playa. *Journal of Geophysical Research*, *106*(D16), 18085–18098. https://doi.org/10.1029/2000JD900324

Gunn, A., Wanker, M., Lancaster, N., Edmonds, D. A., Ewing, R. C., & Jerolmack, D. J. (2021). Circadian rhythm of dune-field activity. *Geophysical Research Letters*, *48*(5), e2020GL090924. https://doi.org/10.1029/2020GL090924

Hersbach, H., Bell, B., Berrisford, P., Biavati, G., Horanyi, A., Munoz Sabater, J., et al. (2018a). ERA5 hourly data on pressure levels from 1979 to present [Dataset]. *Copernicus Climate Change Service (C3S) Climate Data Store (CDS)*. https://doi.org/10.24381/cds.bd0915c6

Hersbach, H., Bell, B., Berrisford, P., Biavati, G., Horanyi, A., Munoz Sabater, J., et al. (2018b). ERA5 hourly data on single levels from 1979 to present [Dataset]. *Copernicus Climate Change Service (C3S) Climate Data Store (CDS)*. https://doi.org/10.24381/cds.adbb2d47

Hersbach, H., Bell, B., Berrisford, P., Biavati, G., Horanyi, A., Munoz Sabater, J., et al. (2019a). ERA5 monthly averaged data on pressure levels from 1979 to present [Dataset]. *Copernicus Climate Change Service (C3S) Climate Data Store (CDS)*. https://doi.org/10.24381/cds.6860a573

Hersbach, H., Bell, B., Berrisford, P., Biavati, G., Horanyi, A., Munoz Sabater, J., et al. (2019b). ERA5 monthly averaged data on single levels from 1979 to present [Dataset]. *Copernicus Climate Change Service (C3S) Climate Data Store (CDS)*. https://doi.org/10.24381/cds.f17050d7

Honda, M., & Shimizu, H. (2002). Geochemical, mineralogical and sedimentological studies on the Taklimakan Desert sands. *Sedimentology*, *45*(6), 1125–1143. https://doi.org/10.1046/j.1365-3091.1998.00202.x

Hugenholtz, C. H., & Barchyn, T. E. (2011). Laboratory and field performance of a laser particle counter for measuring aeolian sand transport. *Journal of Geophysical Research*, *116*(F1), F01010. https://doi.org/10.1029/2010JF001822

Iversen, J. D., & White, B. R. (1982). Saltation threshold on Earth, Mars and Venus. *Sedimentology*, *29*, 111–119.

Jin, L., & He, Q. (2023). On the association between fine dust concentrations from sand dunes and environmental factors in the Taklimakan Desert. *Remote Sensing*, *15*(7), 1719. https://doi.org/10.3390/rs15071719

Kesti, J., Backman, J., O'Connor, E. J., Hirsikko, A., Asmi, E., Aurela, M., et al. (2022). Aerosol particle characteristics measured in the United Arab Emirates and their response to mixing in the boundary layer. *Atmospheric Chemistry and Physics*, *22*(1), 481–503. https://doi.org/10.5194/acp-22-481-2022

Kok, J. F., & Renno, N. O. (2006). Enhancement of the emission of mineral dust aerosols by electric forces. *Geophysical Research Letters*, *33*(19), L19S01. https://doi.org/10.1029/2006gl026284

Kumar, K. N., Entekhabi, D., & Molini, A. (2015). Hydrological extremes in hyperarid regions: A diagnostic characterization of intense precipitation over the central Arabian Peninsula. *Journal of Geophysical Research*, *120*(5), 1637–1650. https://doi.org/10.1002/2014jd022341

Kurosaki, K., & Mikami, M. (2007). Threshold wind speed for dust emission in east Asia and its seasonal variations. *Journal of Geophysical Research*, *112*(D17), D17202. https://doi.org/10.1029/2006JD007988

LeGrande, S. L., Letcher, T. W., Okin, G. S., Webb, N. P., Gallagher, A. R., Dhital, S., et al. (2023). Application of a satellite-retrieved sheltering parameterization (v1.0) for dust event simulation with WRF-Chem v4.1. *Goescientific Model Development*, *16*(3), 1009–1038. https://doi.org/10.5194/gmd-16-1009-2023

Li, Y., & Sadr, R. (2023). Atmospheric turbulent characteristics under summer Shamal in coastal Qatar. *Journal of Geophysical Research: Atmospheres*, *128*(10), e2022JD037971. https://doi.org/10.1029/2022JD037971

Machado, L. A. T., Rossow, W. B., Guedes, R. L., & Walker, A. W. (1998). Life cycle variations of mesoscale convective systems over the Americas. *Monthly Weather Review*, *126*(6), 1630–1654. https://doi.org/10.1175/1520-0493(1998)126

Mahowald, N., Albani, S., Kok, J. F., Engelstaeder, S., Scanza, R., Ward, D. S., & Flanner, M. G. (2014). The size distribution of desert dust aerosols and its impact on the Earth system. *Aeolian Research*, *15*, 53–71. https://doi.org/10.1016/j.aeolia.2013.09.002

Mahto, S. S., & Mishra, V. (2019). Does ERA-5 outperform other reanalysis products for hydrologic applications in India? *Journal of Geophysical Research: Atmospheres*, *124*(16), 9423–9441. https://doi.org/10.1029/2019JD031155

Marticorena, B., & Bergametti, G. (1995). Modeling the atmospheric dust cycle: 1. Design of a soil-derived dust emission scheme. *Journal of Geophysical Research*, *100*(D8), 16415–16430. https://doi.org/10.1029/95JD00690

Nelli, N. (2023). Dataset for the research article entitled "New insights on the Empty Quarter desert environment derived from the WInd-blown Sand Experiment (WISE)" [Dataset]. *Zenodo*. https://doi.org/10.5281/zenodo.10400629

Nelli, N., Fissehaye, S., Francis, D., Fonseca, R., Temimi, M., Weston, M., et al. (2021). Characteristics of atmospheric aerosols over the UAE inferred from CALIPSO and sun photometer aerosol optical depth. *Earth and Space Science*, *8*(6), e2020EA001360. https://doi.org/10.1029/2020EA001360

Nelli, N., Francis, D., Fonseca, R., Bosc, E., Addad, Y., Temimi, M., et al. (2022). Characterization of the atmospheric circulation near the Empty Quarter Desert during major weather events. *Frontiers in Environmental Science*, *10*, 972380. https://doi.org/10.3389/fenvs.2022.972380

Nelli, N., Francis, D., Fonseca, R., Masson, O., Sow, M., & Bosc, E. (2024). First measurements of electric field variability during fog events in the United Arab Emirates. *Journal of Arid Environments*, *220*, 105096. https://doi.org/10.1016/j.jaridenv.2023.105096

Nelli, N. R., Francis, D., Fonseca, R. M., Abida, R., Weston, M., Wehbe, Y., & Al Hosary, T. (2021). The atmospheric controls of extreme convective events over the southern Arabian Peninsula during the spring season. *Atmospheric Research*, *262*, 105778. https://doi.org/10.1016/j.atmosres.2021.105788

Nelli, N. R., Temimi, M., Fonseca, R. M., Weston, M. J., Thota, M. S., Valappil, V. K., et al. (2020a). Impact of roughness length on WRF simulated land-atmosphere interactions over a hyper-arid region. *Earth and Space Science*, *7*(6), e2020EA001165. https://doi.org/10.1029/2020EA001165

Nelli, N. R., Temimi, M., Fonseca, R. M., Weston, M. J., Thota, M. S., Valappil, V. K., et al. (2020b). Micrometeorological measurements in an arid environment: Diurnal characteristics and surface energy balance closure. *Atmospheric Research*, *234*, 104745. https://doi.org/10.1016/j.atmosres.2019.104745

Nesterov, O., Temimi, M., Fonseca, R., Narendra, N., Addad, Y., Bosc, E., & Abida, R. (2021). Validation and statistical analysis of group for high resolution sea surface temperatures (GHRSST) data in the Arabian Gulf. *Oceanologia*, *63*(4), 497–515. https://doi.org/10.1016/j.oceano.2021.07.001

Notaro, M., Alkolibi, F., Fadda, E., & Bakhrjy, F. (2013). Trajectory analysis of Saudi Arabian dust storms. *Journal of Geophysical Research: Atmospheres*, *118*(12), 6028–6043. https://doi.org/10.1002/jgrd.503466

Panofsky, H. A., & Townsend, A. A. (1964). Change of terrain roughness and the wind profile. *Quarterly Journal of the Royal Meteorological Society*, *91*(388), 147–155. https://doi.org/10.1002/qj.49709138818

Park, S. U., & In, H. J. (2003). Parameterization of dust emission for the simulation of the yellow sand (Asian dust) event observed in March 2002 in Korea. *Journal of Geophysical Research*, *108*(D19), 4618. https://doi.org/10.1029/2003JD003484

Pastore, G., Baird, T., Vermeesch, P., Bristow, C., Resentini, A., & Garzanti, E. (2021). Provenance and recycling of Sahara Desert sand. *Earth-Science Reviews*, *216*, 103606. https://doi.org/10.1016/j.earscirev.2021.103606

Rao, K. G., Narendra Reddy, N., Ramakrishna, G., Bhuyan, P. K., Bhuyan, K., Kalita, G., & Pathak, B. (2013). Near surface atmospheric response to the total solar Eclipse at dibrugarh on 22 July 2009. *Journal of Atmospheric and Solar-Terrestrial Physics*, *95–96*, 87–95. https://doi.org/10.1016/j.jastp.2013.01.001

Rao, K. G., & Reddy, N. N. (2019). On moisture flux of the Indian summer monsoon: A new perspective. *Geophysical Research Letters*, *46*(3), 1794–1804. https://doi.org/10.1029/2018GL080392

Reddy, N. N., & Rao, K. G. (2016). Roughness lengths at four stations within the micrometeorological network over the Indian monsoon region. *Boundary-Layer Meteorology*, *158*(1), 151–164. https://doi.org/10.1007/s10546-015-0080-2

Reddy, N. N., & Rao, K. G. (2018). Contrasting variations in the surface layer structure between the convective and non-convective periods in the summer monsoon season for Bangalore location during PRWONAM. *Journal of Atmospheric and Solar-Terrestrial Physics*, *167*, 156–168. https://doi.org/10.1016/j.jastp.2017.11.017

Rehman, S. (2010). Temperature and rainfall variation over Dhahran, Saudi Arabia, (1970–2006). *International Journal of Climatology*, *30*(3), 445–449. https://doi.org/10.1002/joc.1907

Ryder, C. L., Highwood, E. J., Rosenberg, P. D., Trembath, J., Brooke, J. K., Bart, M., et al. (2013). Optical properties of Saharan dust aerosol and contribution from the coarse mode as measured during the Fennec 2011 aircraft campaign. *Atmospheric Chemistry and Physics*, *13*(1), 303–325. https://doi.org/10.5194/acp-13-303-2015

SENTRYTM. (2019). Visibility sensor user's guide. Retrieved from http://www.duranelectronica.com/english/wp-content/uploads/2015/12/ISVS1-T-Users-Guide-Jan-2013-opac-v02.pdf

Shao, Y., Ishizuka, M., Mikami, M., & Leys, J. F. (2011). Parameterization of size-resolved dust emission and validation with measurements. *Journal of Geophysical Research*, *116*(D8), D08203. https://doi.org/10.1029/2010JD014527

Sherman, D. J., Li, B., Farrell, E. J., Ellis, J. T., Cox, W. D., Maia, L. P., & Sousa, P. H. G. O. (2011). Measuring aeolian saltation: A comparison of sensors. *Journal of Coastal Research*, *SI59*, 280–290. https://doi.org/10.2112/SI59-030.1

Skamarock, W. C., Klemp, J. B., Dudhia, J., Gill, D. O., Liu, Z., Berner, J., et al. (2019). Description of the advanced research WRF model version 4.3 (No. NCAR/TN-556+STR). Retrieved from https://opensky.ucar.edu/islandora/object/opensky:2898

Sow, M., Alfaro, S. C., Rajot, J. L., & Marticorena, B. (2009). Size resolved dust emission fluxes measured in Niger during 3 dust storms of the AMMA experiment. *Atmospheric Chemistry and Physics*, *9*(12), 3881–3891. https://doi.org/10.5194/acp-9-3881-2009

Spaan, W. P., & Van den Abeele, G. D. (1991). Wind borne particle measurements with acoustic sensors. *Soil Technology*, *4*(1), 51–53. https://doi.org/10.1016/0933-3630(91)90039-P

Stout, J. E., & Arimoto, R. (2010). Threshold wind velocities for sand movement in the Mescalero Sands of southeastern New Mexico. *Journal of Arid Environments*, *74*(11), 1456–1460. https://doi.org/10.1016/j.jaridenv.2010.05.011

Tan, L., An, Z., Zhang, K., Qu, J., Han, Q., & Wang, J. (2020). Intermittent aeolian saltation over a gobi surface: Threshold, saltation layer height, and high-frequency variability. *Journal of Geophysical Research: Earth Surface*, *125*(1), e2019JF005329. https://doi.org/10.1029/2019JF005329

Taraphdar, S., Pauluis, O. M., Xue, L., Liu, C., Rasmussen, R., Ajayamohan, R. S., et al. (2021). WRF gray zoen simulations of precipitation over the Middle-East and the UAE: Impacts of physical parameterizations and resolution. *Journal of Geophysical Research: Atmospheres*, *126*(10), e201JD034648. https://doi.org/10.1029/2021JD034648

Temimi, M., Fonseca, R., Nelli, N., Weston, M., Thota, M., Valappil, V., et al. (2020). Assessing the impact of changes in land surface conditions on wrf predictions in arid regions. *Journal of Hydrometeorology*, *21*(12), 2829–2853. https://doi.org/10.1175/JHM-D-20-0083.1

Temimi, M., Fonseca, R. M., Nelli, N. R., Valappil, V. K., Weston, M. J., Thota, M. S., et al. (2020). On the analysis of ground-based microwave radiometer data during fog conditions. *Atmospheric Research*, *231*, 104652. https://doi.org/10.1016/j.atmosres.2019.104652

Thota, M. S., Temimi, M., Ajayamohan, R. S., Nelli, N. R., Fonseca, R. M., Weston, M. J., & Valappil, V. (2020). On the investigation of the typology of fog events in an arid environment and the link with climate patterns. *Monthly Weather Review*, *148*(8), 3181–3202. https://doi.org/10.1175/MWR-D-20-0073.1

Todd, M. C., Bou Karam, D., Cavazos, C., Bouet, C., Heinold, B., Baldasano, J. M., et al. (2008). Quantifying uncertainty in estimates of mineral dust flux: An intercomparison of model performance over the Bodélé Depression, northern Chad. *Journal of Geophysical Research*, *113*(D24), D24107. https://doi.org/10.1029/2008JD010476

Uno, I., Amano, H., Emori, S., Kinoshita, K., Matsui, I., & Sugimoto, N. (2001). Trans-Pacific yellow sand transport observed in April 1998: Anumerical simulation. *Journal of Geophysical Resesearch*, *106*(D16), 18331–18344. https://doi.org/10.1029/2000JD900748

Washington, R., & Todd, M. C. (2005). Atmospheric controls on mineral dust emission from the Bodélé Depression, Chad: Intraseasonal to interannual variability and the role of the Low Level Jet. *Geophysical Research Letters*, *32*(17), L17701. https://doi.org/10.1029/2005GL023597

Weston, M. J., Francis, D., Nelli, N., Fonseca, R., Temimi, M., & Addad, Y. (2022). The first characterization of fog Microphysics in the United Arab Emirates, an arid region on the Arabian Peninsula. *Earth and Space Science*, *9*(2), e2021EA002032. https://doi.org/10.1029/2021EA002032

Weston, M. J., & Temimi, M. (2020). Application of a nighttime fog detection method using SEVIRI over an arid environment. *Remote Sensing*, *12*(14), 2281. https://doi.org/10.3390/rs12142281

Weston, M. J., Temimi, M., Nelli, N. R., Fonseca, R. M., Thota, M. S., & Valappil, V. K. (2021). On the analysis of the low-level Double temperature inversion over the United Arab Emirates: A case study during April 2019. *IEEE Geoscience and Remote Sensing Letters*, *18*(2), 346–350. https://doi.org/10.1109/LGRS.2020.2972597

Yang, K., Koike, T., Ishikawa, H., Kim, J., Li, X., Liu, H., et al. (2008). Turbulent flux transfer over bare-soil surfaces: Characteristics and parameterization. *Journal of Applied Meteorology and Climatology*, *47*(1), 276–290. https://doi.org/10.1175/2007JAMC1547.1

Yang, X., He, Q., Liu, X., Yang, F., Huo, W., Shen, S., & Mimtimin, A. (2018). Saltation activity and its threshold velocity in the Gurbantunggut Desert, China. *Natural Hazards*, *90*(1), 349–364. https://doi.org/10.1007/s11069-017-3047-4

Yang, X. H., He, Q., Mamtimin, A., Huo, W., & Liu, X. (2013). Diurnal variations of saltation activity at Tazhong: The hinterland of Taklimakan Desert. *Meteorology and Atmospheric Physics*, *119*(3–4), 177–185. https://doi.org/10.1007/s00703-012-0227-3

Yu, Y., Notaro, M., Kalashnikova, O. V., & Garay, M. J. (2016). Climatology of summer Shamal wind in the Middle East. *Journal of Geophysical Research: Atmospheres*, *121*(1), 289–305. https://doi.org/10.1002/2015jd024063